The CMSSM and NUHM1 in Light of 7 TeV LHC, $B_s \to \mu^+\mu^-$ and XENON100 Data

O. Buchmueller[a], **R. Cavanaugh**[b,c], **M. Citron**[a], **A. De Roeck**[d,e], **M.J. Dolan**[f], **J.R. Ellis**[g,d], **H. Flächer**[h], **S. Heinemeyer**[i], **G. Isidori**[j,d], **J. Marrouche**[a], **D. Martínez Santos**[d], **S. Nakach**[a], **K.A. Olive**[k], **S. Rogerson**[a], **F.J. Ronga**[l], **K.J. de Vries**[a], **G. Weiglein**[m]

[a]High Energy Physics Group, Blackett Laboratory, Imperial College, Prince Consort Road, London SW7 2AZ, UK

[b]Fermi National Accelerator Laboratory, P.O. Box 500, Batavia, Illinois 60510, USA

[c]Physics Department, University of Illinois at Chicago, Chicago, Illinois 60607-7059, USA

[d]Physics Department, CERN, CH–1211 Genève 23, Switzerland

[e]Antwerp University, B–2610 Wilrijk, Belgium

[f]Institute for Particle Physics Phenomenology, University of Durham, South Road, Durham DH1 3LE, UK

[g]Theoretical Particle Physics and Cosmology Group, Department of Physics, King's College London, London WC2R 2LS, UK

[h]H.H. Wills Physics Laboratory, University of Bristol, Tyndall Avenue, Bristol BS8 1TL, UK

[i]Instituto de Física de Cantabria (CSIC-UC), E–39005 Santander, Spain

[j]INFN, Laboratori Nazionali di Frascati, Via E. Fermi 40, I–00044 Frascati, Italy

[k]William I. Fine Theoretical Physics Institute, School of Physics and Astronomy, University of Minnesota, Minneapolis, Minnesota 55455, USA

[l]Institute for Particle Physics, ETH Zürich, CH–8093 Zürich, Switzerland

[m]DESY, Notkestrasse 85, D–22607 Hamburg, Germany

We make a frequentist analysis of the parameter space of the CMSSM and NUHM1, using a Markov Chain Monte Carlo (MCMC) with 95 (221) million points to sample the CMSSM (NUHM1) parameter spaces. Our analysis includes the ATLAS search for supersymmetric jets + $\not{E}_T$ signals using ~ 5/fb of LHC data at 7 TeV, which we apply using `PYTHIA` and a `Delphes` implementation that we validate in the relevant parameter regions of the CMSSM and NUHM1. Our analysis also includes the constraint imposed by searches for BR($B_s \to \mu^+\mu^-$) by LHCb, CMS, ATLAS and CDF, and the limit on spin-independent dark matter scattering from 225 live days of XENON100 data. We assume $M_h \sim 125$ GeV, and use a full set of electroweak precision and other flavour-physics observables, as well as the cold dark matter density constraint. The $\text{ATLAS}_{5/\text{fb}}$ constraint has relatively limited effects on the 68 and 95% CL regions in the $(m_0, m_{1/2})$ planes of the CMSSM and NUHM1. The new BR($B_s \to \mu^+\mu^-$) constraint has greater impacts on these CL regions, and also impacts significantly the 68 and 95% CL regions in the $(M_A, \tan\beta)$ planes of both models, reducing the best-fit values of $\tan\beta$. The recent XENON100 data eliminate the focus-point region in the CMSSM and affect the 68 and 95% CL regions in the NUHM1. In combination, these new constraints reduce the best-fit values of $m_0, m_{1/2}$ in the CMSSM, and increase the global χ^2 from 31.0 to 32.8, reducing the p-value from 12% to 8.5%. In the case of the NUHM1, they have little effect on the best-fit values of $m_0, m_{1/2}$, but increase the global χ^2 from 28.9 to 31.3, thereby reducing the p-value from 15% to 9.1%.

KCL-PH-TH/2012-26, LCTS/2012-13, CERN-PH-TH/2012-164,
DCPT/12/82, DESY 12-115, IPPP/12/41, FTPI-MINN-12/20, UMN-TH-3106/12

1. Introduction

The LHC searches for jets $+\not{E}_T$ events, as well as searches for heavy Higgs bosons H/A and the rare decay $B_s \to \mu^+\mu^-$, are placing ever-stronger constraints on supersymmetric models, in particular those in which R-parity is conserved and the lightest neutralino $\tilde{\chi}_1^0$ is the stable lightest supersymmetric particle and provides the cosmological dark matter. There have been a number of analyses of the constraints imposed by ATLAS and CMS using ~ 1/fb at 7 TeV [1–3] and other data on the parameter spaces of simplified versions of the minimal supersymmetric extension of the Standard Model (MSSM) [4], particularly the constrained MSSM (CMSSM) [5] in which the soft supersymmetry-breaking parameters m_0, $m_{1/2}$ and A_0 are universal at the GUT scale, and some also of the LHC constraints on models in which the soft supersymmetry-breaking contributions to the masses of the Higgs multiplets are non-universal but equal to each other, the NUHM1 models [6]. There have also been analyses of the CMSSM and NUHM1 of the prospective implications of a Higgs boson weighing $\sim$ 125 GeV [2, 7–10], and analyses within the CMSSM and NUHM1 [8–11] that incorporate LHC searches for jets $+\not{E}_T$ events with ~ 5/fb of LHC data at 7 TeV [12, 13]. Here we extend our previous frequentist analyses of the CMSSM and NUHM1 [1, 2, 14–20] to include the ATLAS jets $+\not{E}_T$ results with ~ 5/fb [12] of data as well as $M_h \sim 125$ GeV and recent data on BR($B_s \to \mu^+\mu^-$) from the ATLAS [21], CDF [22], CMS [23] and LHCb [24] Collaborations [25], and the recent CMS exclusion of $H/A \to \mu^+\mu^-$ [26]. We also implement the constraint on the spin-independent dark matter scattering cross section imposed by 225 live days of XENON100 data [27]. We give a critical discussion of the extent to which the CMSSM and NUHM1 can be said to be disfavoured by the available data from the LHC and elsewhere.

The results of experimental searches for jets $+\not{E}_T$ events are typically presented within the framework of the CMSSM for some fixed A_0 and $\tan\beta$. The applicability of these analyses to other A_0 and $\tan\beta$ values, as well as to constraining the NUHM1, requires some study and justification. Within the CMSSM, one must verify that the constraints used are indeed independent of A_0 and $\tan\beta$, as often stated in the experimental papers on searches for jets $+\not{E}_T$ events. Similarly, within the NUHM1 one must verify whether, for any specific set of values of m_0, $m_{1/2}$, A_0 and $\tan\beta$, the sensitivities of ATLAS and CMS searches for jets $+\not{E}_T$ events might depend on the degree of non-universality in the NUHM1. A second issue arising in the NUHM1 is that the range of m_0 that is consistent with the $\tilde{\chi}_1^0$ LSP requirement depends on the degree of non-universality. In the CMSSM, for any given value of $m_{1/2}$ there is a lower limit on m_0 that is, in general, violated in the NUHM1. Since the LHC experiments generally quote results only for the region of the $(m_0, m_{1/2})$ plane allowed within the CMSSM, a dedicated study is needed to estimate the correct extrapolation of LHC results outside this region.

In order to explore the sensitivity to more general CMSSM and NUHM parameters of the published LHC searches for supersymmetry within specific CMSSM models, we use a version of the `Delphes` [28] generic simulation package with a 'card' that emulates the performance of the ATLAS detector. As described below, in the specific case of the 7 TeV ATLAS 5/fb jets $+\not{E}_T$ analysis, `Delphes` reproduces reasonably accurately the quoted 95% CL limits on CMSSM models with $A_0 = 0$ and $\tan\beta = 10$, as well as other confidence levels in the CMSSM $(m_0, m_{1/2})$ plane. These are well described by scaling of event numbers $\propto 1/\mathcal{M}^4$, where $\mathcal{M} \equiv \sqrt{m_0^2 + m_{1/2}^2}$, as assumed in [1]. We also use the `Delphes` simulation to confirm that the ATLAS 5/fb jets $+\not{E}_T$ constraint in the $(m_0, m_{1/2})$ plane of the CMSSM is relatively insensitive to $\tan\beta$ and A_0.

Having validated the application of the `Delphes` simulation to the CMSSM, we then study whether the results of [12] are sensitive to the degree of Higgs non-universality in the NUHM1. Although the supersymmetric decay cascades to which this analysis is most sensitive are independent of the details of the supersymmetric Higgs sector, they do in principle have some sensitivity to the Higgs mixing parameter μ,

which is in general different in the NUHM1 from its value in the CMSSM. We find that in practice the jets + $\not{E}_T$ constraint is essentially independent of the degree of non-universality in the NUHM1. We then use `Delphes` to estimate the sensitivity of the ATLAS analysis to the region with m_0 smaller than is allowed in the CMSSM, finding that the ATLAS jets + $\not{E}_T$ constraint is essentially independent of m_0 in this range.

Following these validations of our implementation of `Delphes` in the NUHM1, we use the Markov Chain Monte Carlo (MCMC) technique to sample the CMSSM and NUHM1 parameter spaces with $\sim 95 \times 10^6$ and $\sim 221 \times 10^6$ points, respectively. Given the constraints from M_h and the $\mathrm{LHC}_{1/\mathrm{fb}}$ data, we find that the ATLAS 5/fb jets + $\not{E}_T$ constraint by itself has a relatively limited impact on the 68 and 95% CL regions in the $(m_0, m_{1/2})$ planes of the CMSSM and NUHM1, whereas the new $\mathrm{BR}(B_s \to \mu^+\mu^-)$ constraint has larger effects in both these and the $(M_A, \tan\beta)$ planes, and the new XENON100 constraint also impacts significantly both the $(m_0, m_{1/2})$ and $(M_A, \tan\beta)$ planes of the CMSSM and NUHM1. After the inclusion of these constraints, we find that in the favoured regions in the CMSSM and NUHM1 in m_0, $m_{1/2}$ and $\tan\beta$ the global χ^2 function varies little, giving less relevance to the best-fit values of these parameters. Nevertheless, we note that the best-fit values of m_0 and $m_{1/2}$ are decreased in the CMSSM, and the best-fit values of $\tan\beta$ are decreased in both the CMSSM and the NUHM1. Within the CMSSM, the global χ^2 increases from 31.0 to 32.8 and the p-value is correspondingly reduced from 12% to 8.5%. Within the NUHM1, the value of $\tan\beta$ rises to a value similar to that in the CMSSM, while the total χ^2 rises from 28.9 to 31.3, reducing the p-value from 15% to 9.1%. The perilously low p-values of the CMSSM and NUHM1 reflect the growth in tension between LHC constraints and low-energy measurements such as $(g-2)_\mu$ [29, 30].

2. Analysis Procedure

We follow closely the procedure described in [1]. As in [1], the sampling is based on the Metropolis-Hastings algorithm, with a multi-dimensional Gaussian distribution as proposal density. The width of this distribution is adjusted during the sampling, so as to keep the MCMC acceptance rate between 20% and 40% in order to ensure efficient sampling. We emphasize that we do not make use of the sampling density to infer the underlying probability distribution. Rather, we use the MCMC method to construct a global likelihood function that receives contributions from the usual full set of electroweak precision observables including $(g-2)_\mu$ [29], measurements of $\mathrm{BR}(b \to s\gamma)$, $\mathrm{BR}(B_u \to \tau\nu_\tau)$, $\mathrm{BR}(B_s \to \mu^+\mu^-)$, B-meson mixing and other flavour-physics observables [25, 31], the cosmological $\tilde{\chi}_1^0$ density and the XENON100 direct search for dark matter scattering [32], as well the LHC searches for the Higgs boson and supersymmetric signals.

Our treatment of the non-LHC constraints is similar to that in [1], with the exceptions that we use updated values of $M_W = 80.385 \pm 0.015$ GeV [33] and $m_t = 173.2 \pm 0.9$ GeV [34]. Our treatment of $\mathrm{BR}(B_s \to \mu^+\mu^-)$ is based on a compilation of the recent measurements by ATLAS [21], CDF [22], CMS [23] and LHCb [24, 25]. As already mentioned, we incorporate the public results of the search for jets + $\not{E}_T$ events without leptons using ~ 5/fb of LHC data at 7 TeV analyzed by ATLAS [12], which has greater sensitivities to the models discussed here than do searches with leptons and b-quarks in the final state as well as searches with less integrated luminosity. We also include the CMS constraint on the heavier MSSM Higgs bosons, H/A [26], which has greater sensitivity than the corresponding ATLAS search [35].

Concerning the Higgs boson, the situation has evolved rapidly since our previous analysis [2] and the data reported earlier this year [39, 40], with the recently-announced discovery by the CMS [36] and ATLAS Collaborations [37], consistent with evidence from the CDF and D0 Collaborations [38], of a new particle that is a very strong candidate to be a Higgs boson resembling that in the Standard Model. In the absence of an official combination of these results, we model them by assuming, as in [2], that

$$M_h = 125 \pm 1 \text{ (exp.)} \pm 1.5 \text{ (theo.) GeV} , \qquad (1)$$

and we incorporate this new constraint using the same 'afterburner' approach as in [2].

The contributions of these observables to the global likelihood function are calculated within the `MasterCode` framework [41]. This incorporates a code for the electroweak observables based on [42] as well as the `SoftSUSY` [43], `FeynHiggs` [44], `SuFla` [45], and `MicrOMEGAs` [46] codes, interfaced via the SUSY Les Houches Accord [47]. We use the `SuperIso` [48] and `SSARD` [49] codes as comparisons for B-physics observables [1] and for the cold dark matter density, using also `DarkSUSY` [50] as a comparison for the latter. We use `SSARD` for the spin-independent dark matter scattering cross section, comparing with `MicrOMEGAs` and `DarkSUSY`.

3. Validation and Extension of Jets + $\not{E}_T$ Constraints

ATLAS and CMS results on SUSY searches for jets $+\not{E}_T$ are typically shown as 95% CL exclusion bounds in the CMSSM $(m_0, m_{1/2})$ plane for fixed $\tan\beta$ and A_0, e.g., $\tan\beta = 10$ and $A_0 = 0$ [12, 53]. We first validate for these values of $\tan\beta$ and A_0 our implementation of the ATLAS constraint using `PYTHIA` [54] and the generic `Delphes` [28] simulation code with an ATLAS detector 'card'. Next we extend it to other values of the CMSSM parameters, and then to the NUHM1 [2].

Validation in the $(m_0, m_{1/2})$ plane

As a first step in the validation procedure, we used `SoftSUSY` [43] to generate the spectra for various points in the $(m_0, m_{1/2})$ plane of the CMSSM for $\tan\beta = 10$ and $A_0 = 0$. We then used `PYTHIA` [54] to generate 50,000 events for each of these points, which were subsequently passed through the `Delphes` [28] simulation code using the ATLAS detector 'card'. We then used information from [12] to calculate the efficiencies for observing events that would survive the cuts used in the ATLAS jets + $\not{E}_T$ analysis using 5/fb of data at 7 TeV. Taking into account the observed number of events, together with the information in Table 3 of [12], we then calculated the confidence levels of these points, using the same prescription as ATLAS. We recall that the ATLAS analysis combined searches using several different channels A, A', B, C, D and E, which, depending on the channel, may have 'tight', 'medium' and 'loose' event selections. Following the procedure used in the ATLAS analysis, for each set of CMSSM parameters we used the limit set by the most sensitive of these various channel selections.

The left panel of Fig. 1 displays how closely this work flow reproduced the ATLAS CL for 34 test points along its 95% CL exclusion line, sampling the range $m_0 \in (200, 3500)$ GeV in 100 GeV steps. Our results indicate a mean difference $\mathrm{CL}_{\texttt{Delphes}}$ - $\mathrm{CL}_{\mathrm{ATLAS}} = (-2.8 \pm 3.6)\%$, so we conclude that our simulation using `PYTHIA` and `Delphes` reproduces quite accurately the 95% CL exclusion contour in the $(m_0, m_{1/2})$ plane for $\tan\beta = 10$ and $A_0 = 0$ reported by ATLAS.

Since it is not computationally feasible to use `PYTHIA` and `Delphes` in this way for every point generated in our MCMC analysis, we make use of a simple analytic approximation to their results in order to extrapolate their results to other regions of the $(m_0, m_{1/2})$ plane. The right panel of Fig. 1 compares the CL values estimated using this `Delphes` implementation, for a number of CMSSM points with $\tan\beta = 10$, $A_0 = 0$ and varying m_0 and $m_{1/2}$, with the CL calculated assuming, as in [1], that the numbers of events for different points in the CMSSM $(m_0, m_{1/2})$ plane scale as $1/\mathcal{M}^4$ (solid line). We see that the agreement is quite good along rays in the $(m_0, m_{1/2})$ plane with $m_{1/2}/m_0 = 1/3$ (blue circles), 1 (red squares) and 3 (green triangles), indicating that this scaling law is an adequate approximation to the true sensitivity of the ATLAS 5/fb jets + $\not{E}_T$ analysis.

[1] We do not include the isospin asymmetry in $B \to K^{(*)}\mu^+\mu-$ decays [51] or the measurement of BR($B \to D^{(*)}\tau\nu$) [52] in our analysis, in view of the present experimental and theoretical (long-distance) uncertainties.

[2] We have made a similar validation analysis for the CMS α_T search for jets + $\not{E}_T$ events using ~ 1/fb of data at 7 TeV [53]. We do not discuss this validation in detail, as it does not contribute to the the likelihood function analyzed here, but it does validate *a posteriori* our previous treatments [1,2] of the CMS α_T analysis. It also indicates that the CMS sensitivity with 5/fb of data at 7 TeV [13] is similar to the ATLAS 5/fb jets + $\not{E}_T$ data discussed here.

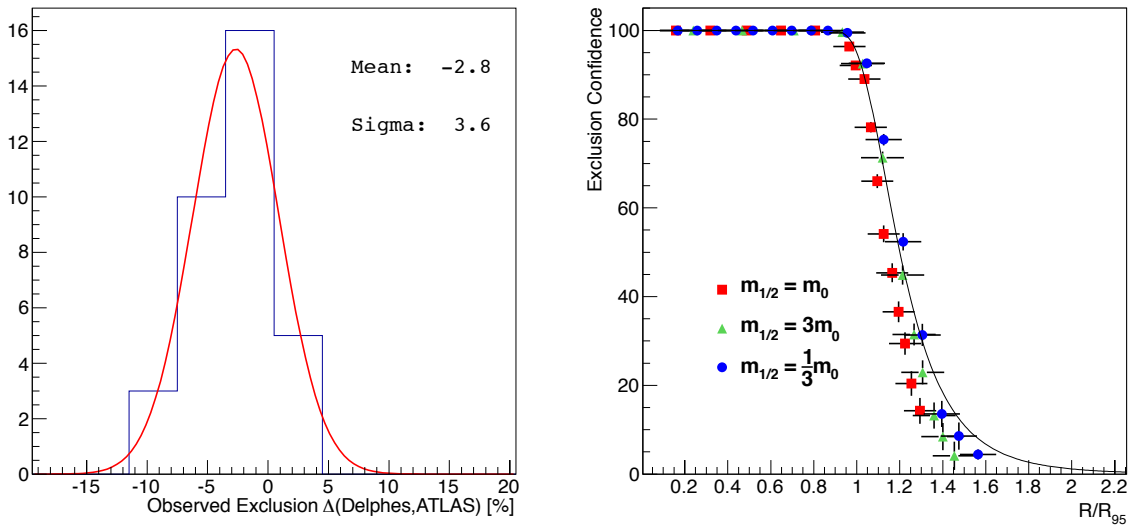

Figure 1. *Left panel: A histogram of the differences between the confidence levels (CLs) we calculate using* `PYTHIA` *and* `Delphes` *from the values quoted by ATLAS for 34 points along the 95% exclusion contour in the* $(m_0, m_{1/2})$ *plane of the CMSSM with* $\tan\beta = 10$ *and* $A_0 = 0$*. The mean difference is* $CL_{\texttt{Delphes}}$ *-* $CL_{\rm ATLAS} = (-2.8 \pm 3.6)\%$*. Right panel: The points are the confidence levels for a selection of CMSSM points with* $\tan\beta = 10$ *and* $A_0 = 0$ *and various values of* $R \equiv \mathcal{M}/\mathcal{M}_0$*, where* $\mathcal{M} \equiv \sqrt{m_0^2 + m_{1/2}^2}$ *and* $\mathcal{M}_0$ *is the value of* $\mathcal{M}$ *at the point on the LHC jets +* $\not{E}_T$ *95% exclusion line with the same ratio* $m_0/m_{1/2}$*. The red squares (blue circles, green triangles) were chosen along rays in the* $(m_0, m_{1/2})$ *plane with* $m_0/m_{1/2} = 1/3, 1, 3$*, respectively. These points compare well with the solid line, which is the CL calculated assuming that the number of signal events surviving the LHC cuts scales as* $1/\mathcal{M}^4$*.*

Extension to other $\tan\beta$ *and* A_0 *values*

The next step is to use our `Delphes` implementation to evaluate the sensitivity of the ATLAS analysis to other values of $\tan\beta$ and A_0. To this end, for each of the 34 points along the 95% CL contour in the $(m_0, m_{1/2})$ plane for $\tan\beta = 10$ and $A_0 = 0$ mentioned previously, we used `PYTHIA` and `Delphes` to estimate the confidence levels of these points as the other parameters are varied, as shown in Fig. 2. The left panel exhibits the variation of the confidence level with $\tan\beta$ for fixed $A_0 = 0$. We see that the CL is quite stable, with its central value ranging between 95 and 90% and its 68% CL range lying between 99% and 84% and always including the 95% CL found by ATLAS for $\tan\beta = 10$ and $A_0 = 0$ [3]. The right panel of Fig. 2 displays a similar analysis for varying $A_0/m_0 \in [-3, 3]$ with $\tan\beta$ fixed at 10. We see again that the CL is quite stable, with central values between 95 and 92% and the 68% CL ranges lying between 100% and 88% and again always including the 95% CL found by ATLAS for $\tan\beta = 10$ and $A_0 = 0$. These results are consistent with the statement by ATLAS [12] that their $(m_0, m_{1/2})$ exclusion contours are largely independent of $\tan\beta$ and A_0, as we have assumed previously [1], and also provide consistency checks on our `Delphes` implementation.

[3] The different sizes of the error bars, here and in subsequent validation plots, are due to `PYTHIA` failing for varying numbers of points.

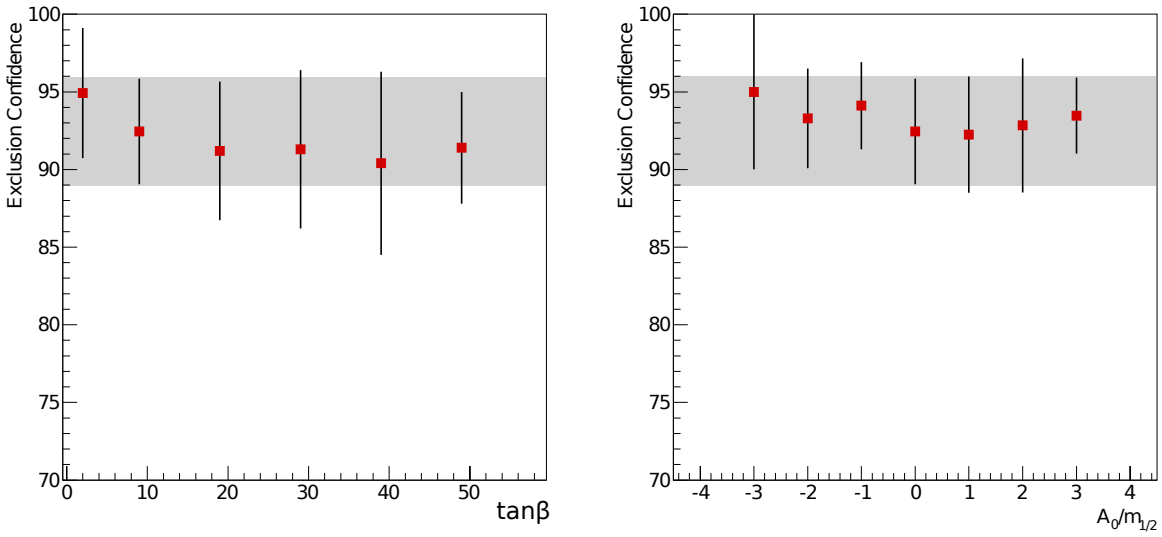

Figure 2. *Calculations using* `Delphes` *of the average and spread in exclusion confidence levels of 34 CMSSM points selected to have the same* $(m_0, m_{1/2})$ *values as points on the 95% ATLAS 5/fb jets +* $\not{E}_T$ *exclusion line for* $\tan\beta = 10$ *and* $A_0 = 0$*, but with different values of* $\tan\beta$ *(left panel) and* A_0 *(right panel). The CL is almost independent of these parameters, with the error bar always embracing 95%. The band represents the* $\pm 1\sigma$ *range of the fit shown in the left panel of Fig. 1.*

Extensions to Non-Universal Higgs Masses

Following these validations, as a third step we now use our `Delphes` implementation to extend the interpretation of the ATLAS 5/fb jets + $\not{E}_T$ analysis to models with non-universal Higgs masses. We recall that in the CMSSM, the electroweak vacuum conditions can be used to fix the Higgs mixing parameter μ and M_A for any given choice of the parameters $m_0, m_{1/2}, A_0$ and $\tan\beta$. Introducing the single extra degree of freedom $m^2_{H_u}/m^2_0 = m^2_{H_d}/m^2_0$ in the NUHM1, one can treat either μ or M_A as a free parameter, whereas these quantities may be treated as two free parameters in the NUHM2, in which $m^2_{H_u}/m^2_0$ and $m^2_{H_d}/m^2_0$ are treated as two independent parameters [55]. The effects of varying μ and M_A on the gluino mass and the spectra of squarks (the main sparticles expected to be produced at the LHC) are of secondary importance [4]. However, they may also affect the branching fractions of the cascade decays to which the LHC experiments are sensitive, and so could in principle have some effect on the sensitivity of the ATLAS 5/fb jets + $\not{E}_T$ search in the $(m_0, m_{1/2})$ plane.

For this reason, we have taken the same 34 points along the 95% CL contour in the $(m_0, m_{1/2})$ for $\tan\beta = 10$ and $A_0 = 0$ studied above, and used `PYTHIA` and `Delphes` to estimate how the confidence levels of these points vary as the Higgs non-universality parameters $m^2_{H_u}/m^2_0$ and $m^2_{H_d}/m^2_0$ are varied. The red squares in the left panel of Fig. 3 show how the CL depends on the common non-universality parameter $m^2_{H_u}/m^2_0 = m^2_{H_d}/m^2_0$ in the NUHM1. As before, we see that the CL does not depart sig-

[4] Except that varying μ affects the masses and mixings of third-generation squarks, but the dominant LHC jets + $\not{E}_T$ searches are less sensitive to these.

nificantly from the CMSSM value of 95%. Also shown in the left panel of Fig. 3 (as blue circles) are PYTHIA and Delphes estimates of the confidence levels of points with the same values of $m_0, m_{1/2}, \tan\beta = 10$ and $A_0 = 0$ but with Higgs non-universality parameters of opposite signs for the two Higgs doublets: $m^2_{H_u}/m^2_0 = -m^2_{H_d}/m^2_0$. The right panel of Fig. 3 shows how the CL in the NUHM2 varies as a function of $m^2_{H_d}$ for fixed $m^2_{H_u} = 0$ (red squares) and as a function of $m^2_{H_u}$ for fixed $m^2_{H_d} = 0$ (blue circles). We again see that the CL is similar to the 95% found in the CMSSM for the same values of $m_0, m_{1/2}, \tan\beta = 10$ and $A_0 = 0$.

Extension to $m_0^2 < 0$

To complete the validation for the NUHM1, and in preparation for future analyses in the NUHM2, we have also investigated the applicability of the ATLAS 5/fb jets $+\not{E}_T$ results to models with smaller values of m_0^2 than in the CMSSM, including negative values. We have evaluated the CL along a line of points with $\tan\beta = 10, A_0 = 0, m_{1/2} = 630$ GeV and $-(150\text{ GeV})^2 < m_0^2 < +(150\text{ GeV})^2$, i.e., $M_0 \equiv \text{sign}(m_0^2) \times \sqrt{|m_0^2|} \in (-150, +150)$ GeV, as shown in Fig. 4. We see that the CL remains constant, within errors, over this range of M_0, and is quite consistent with the 95% CL reported for the ATLAS 5/fb jets $+\not{E}_T$ analysis at $m_0 = 100$ GeV.

4. Combination of BR($B_s \to \mu^+\mu^-$) Constraints

Since our previous analysis [2], new constraints on BR($B_s \to \mu^+\mu^-$) have been published by ATLAS [21], CDF [22], CMS [23] and LHCb [24] Collaborations [25]. Their measurements are to be compared with the theoretical (TH) value in the SM, which we take to be BR($B_s \to \mu^+\mu^-)_{\rm SM,TH} = (3.2 \pm 0.2) \times 10^{-9}$ [57]. This comparison is not direct, because experiments measure the time-averaged (TA) branching ratio, which differs from the TH value because of the difference between the lifetimes of the heavier and lighter B_s mesons [58, 59]. In general, BR($B_s \to \mu^+\mu^-)_{\rm TH} = [(1 - y_s^2)/(1 + \mathcal{A}_{\Delta\Gamma} y_s)] \times$ BR($B_s \to \mu^+\mu^-)_{\rm TA}$, where $\mathcal{A}_{\Delta\Gamma} = +1$ in the SM and $y_s = 0.088 \pm 0.014$. Thus we compare the measurements to the SM prediction for the time-averaged branching ratio: BR($B_s \to \mu^+\mu^-)_{\rm SM,TA}$ = BR($B_s \to \mu^+\mu^-)_{\rm SM,TH}/(1 - y_s) = (3.5 \pm 0.2) \times 10^{-9}$ [59].

We use for this comparison an unofficial combination of the ATLAS, CDF, CMS and LHCb data [21–25], from which we compute a χ^2 penalty for each possible (calculated) value of BR($B_s \to \mu^+\mu^-$). In Fig. 5 we show the probability distribution (left) and the log-likelihood function for the ratio BR($B_s \to \mu^+\mu^-$)/BR($B_s \to \mu^+\mu^-)_{\rm SM,TA}$, folding together the theoretical and experimental errors. The log-likelihood function is used as the $\Delta\chi^2$ penalty for the values of this observable as they are calculated in the CMSSM and NUHM1 [5].

5. The Constraint on Spin-Independent Dark Matter Scattering from 225 Live Days of XENON100 Data

The XENON100 Collaboration has recently published the result of a search for spin-independent dark matter scattering based on 225 live days of data [27]. They report two events in a fiducial region where 1.0 ± 0.2 background events were expected, i.e., no evidence for any excess, quote a 90% CL upper limit of $\sigma_p^{\rm SI} < 2.0 \times 10^{-45}$ cm^2 for a dark matter particle mass of 55 GeV, and provide a 90% CL exclusion line for other masses.

Following the procedure used in [20] for the previous XENON100 constraint, we use a CL$_s$ calculator, now implemented in our Delphes framework, to model the contribution to the global χ^2 function of this new XENON100 constraint from the number of signal events as a Gaussian with mean $\mu = 1.0$ and standard deviation $\sigma = 2.7$ events. This corresponds to the mean (2 - 1 = 1 event) given in [27] and the upper limit of 5.1 signal events at the 90% CL given by the CL$_s$ calculator, which we identify with the published XENON100 90% exclusion line. For models predicting values of $\sigma_p^{\rm SI}$ above or below the 90% CL line in [27], we rescale linearly the number

[5] We note in passing that one expects $\mathcal{A}_{\Delta\Gamma} = +1$ also in these models.

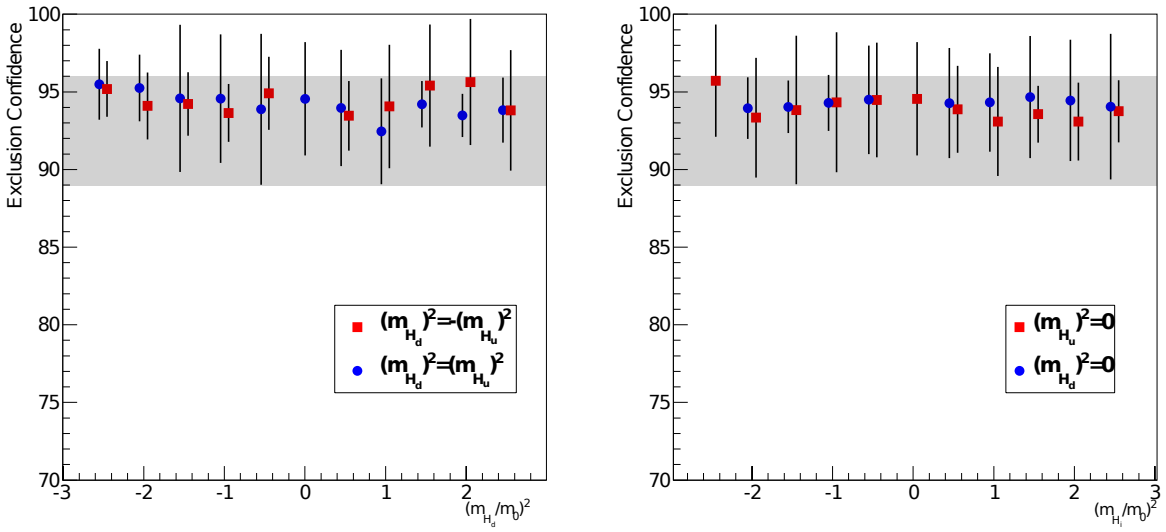

Figure 3. *Calculations using* `Delphes` *of the average and spread in exclusion confidence levels of 34 CMSSM points selected to have the same* $(m_0, m_{1/2})$ *values as points on the 95% LHC jets* $+\not{E}_T$ *exclusion line for* $\tan\beta = 10$ *and* $A_0 = 0$*, as in Fig. 2, but (left panel) varying* $m^2_{H_d}/m^2_0 = m^2_{H_u}/m^2_0$ *in the NUHM1 (red squares) and* $m^2_{H_d}/m^2_0 = -m^2_{H_u}/m^2_0$ *in the NUHM2 (blue circles), and (right panel) varying* $m^2_{H_d}$ *for fixed* $m^2_{H_u} = 0$ *(red squares) and varying* $m^2_{H_u}$ *for fixed* $m^2_{H_d} = 0$ *(blue circles) in the NUHM2. In both panels, the bands represent the* $\pm 1\sigma$ *range of the fit shown in the left panel of Fig. 1.*

of events and estimate the $\Delta\chi^2$ contribution of XENON100 using the Gaussian model described above.

We use `SSARD` [49] to calculate $\sigma_p^{\rm SI}$, assuming a nominal value of the π-N σ term $\Sigma_{\pi N} = 50$ MeV, and assigning an asymmetric error $^{+14}_{-7}$ MeV. This accounts for the fact that $\Sigma_{\pi N} = \sigma_0 \sim 36$ MeV if $\langle N|\bar{s}s|N\rangle = 0$, while allowing for significantly larger values of $\Sigma_{\pi N}$ as suggested by some analyses [60].

The XENON100 analysis assumes that the local dark matter density is 0.3 GeV/cm^3, and makes supplementary assumptions on the dark matter velocity distribution. We have explored the potential implications of the uncertainties in these quantities by convoluting with our above-mentioned model of the XENON100 constraint on $\sigma_p^{\rm SI}$ a fractional uncertainty of a factor $\sqrt{2}^{\pm 1}$ at the 68% CL. We find that it has negligible impact on the results shown below, which are for the nominal dark matter distribution parameters assumed by XENON100.

6. The CMSSM and NUHM1 after ATLAS$_{5/\rm fb}$, BR($B_s \to \mu^+\mu^-$) and XENON100

As already mentioned, in addition to the `Delphes` implementation of the ATLAS 5/fb jets $+\not{E}_T$ constraint, the implementation of the combined BR($B_s \to \mu^+\mu^-$) constraints described above, and the new CMS constraint on $H/A \to \tau^+\tau^-$ [26], we include in our global fit the constraint $M_h = 125 \pm 1.0 \pm 1.5$ GeV and the other constraints included in [2], with updated values of the W boson mass [33] and the top quark mass [34], see above.

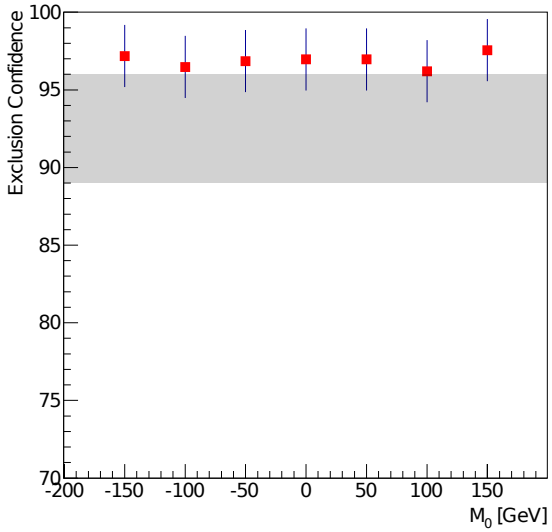

Figure 4. *Calculations using* `Delphes` *of the exclusion confidence levels of NUHM1 points selected to have* $\tan\beta = 10, A_0 = 0, m_{1/2} = (630 \pm 25)$ GeV *and varying* $M_0 = sign(m_0^2) \times \sqrt{|m_0^2|} \in (-150, +150)$ GeV. *The band represents the* $\pm 1\sigma$ *range of the fit shown in the left panel of Fig. 1.*

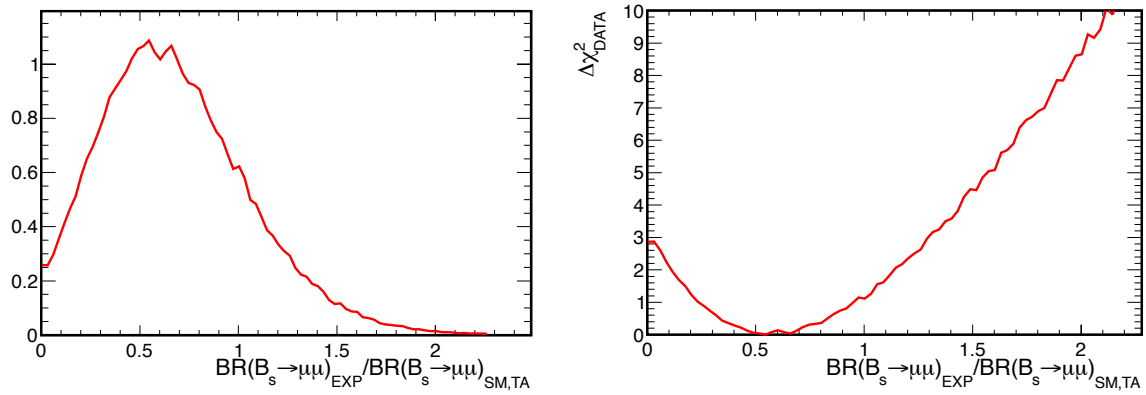

Figure 5. *The probability distribution (left panel) and the log-likelihood function (right panel) found in an unofficial combination of the constraints on* $\mathrm{BR}(B_s \to \mu^+\mu^-)$ *from ATLAS, CDF, CMS and LHCb [21–25], normalized to* $\mathrm{BR}(B_s \to \mu^+\mu^-)_{\mathrm{SM,TA}} = \mathrm{BR}(B_s \to \mu^+\mu^-)_{\mathrm{SM,TH}}/(1 - y_s) = (3.5 \pm 0.2) \times 10^{-9}$, *as described in the text.*

The $(m_0, m_{1/2})$ planes

Fig. 6 displays the $(m_0, m_{1/2})$ planes for the CMSSM (left panel) and the NUHM1 (right panel). The results of the new global fits are shown as solid lines and filled stars, and previous fits based on ~ 1/fb of LHC data are indicated by dashed lines and open stars. The blue and red lines denote levels $\Delta\chi^2 = 2.30$ and 5.99, which we interpret as the 68% and 95% CLs.

We note the existence in the CMSSM of a grouping of points in the focus-point region at large m_0 and small $m_{1/2}$ that were previously allowed at the 95% CL but are now disallowed [6]. This exclusion is due to the new XENON100 constraint [27]. The main effect of the ATLAS 5/fb jets $+ \not{E}_T$ constraint is to shave off a slice of points at low $m_{1/2}$ and moderate m_0. We also note the appearance in the NUHM1 sample of a grouping of points at large $m_{1/2}$ that have smaller m_0 than is possible in the CMSSM, and are allowed at the 95% CL. The relic density in this region is brought into the WMAP range by multiple neutralino and chargino coannihilation processes. Points are found in this region using each of the codes `MicrOMEGAs` [46], `DarkSUSY` [50], `SuperIso` [48] and `SSARD` [49], though they yield somewhat different values of the relic density. As mentioned previously, here we use `MicrOMEGAs` as our default.

The values of χ^2 in the most-favoured regions of the CMSSM and NUHM1 are relatively shallow functions of m_0, $m_{1/2}$ and $\tan\beta$, so that little importance can be attributed to the positions of the best-fit points or to their movements relative to those in [2]. Nevertheless, we note that, as summarized in Table 1, the nominal best-fit point in the CMSSM moves to smaller m_0 and $m_{1/2}$, whereas that in the NUHM1 moves little in this plane. The best-fit points have $\chi^2 = 32.8$ in the CMSSM and 31.3 in the NUHM1, and the p-values of these models are reduced to 8.5 and 9.1%, respectively.

We see in Fig. 6 that the 95% CL region in the CMSSM extends to $m_0 \sim 4000$ GeV and $m_{1/2} \sim 2400$ GeV. The corresponding region in the NUHM1 extends to smaller m_0 but larger $m_{1/2}$. We also note that the CMSSM fit features two disconnected 68% CL 'islands', the one at lower m_0 and $m_{1/2}$ corresponding to the stau coannihilation region, and that at larger m_0 and $m_{1/2}$ corresponding to the rapid-annihilation funnel region. We note, however, that our sampling also includes a few intermediate points that also have $\Delta\chi^2 < 2.30$, reflecting the relative flatness of the global χ^2 function along the band between $(m_0, m_{1/2}) \sim (300, 900)$ GeV and $\sim (1100, 1900)$ GeV. Typically, these points sit in rapid-annihilation funnels, and it is possible that a more complete sampling might reveal a lower 'isthmus' connecting these islands, as happens in the NUHM1.

We report in Table 1 the values of $m_0, m_{1/2}, A_0$ and $\tan\beta$ for the best fits in both the CMSSM 'islands', as well as for the best fit in the NUHM1, which is at relatively low masses, and a local minimum of the NUHM1 χ^2 function at high masses. We note that the best fit in the low-mass CMSSM 'island' is similar to the best fit in the NUHM1, and that both have smaller $\tan\beta$ than in the previous best fits to the $\mathrm{LHC}_{1/\mathrm{fb}}$ data set in these models. As we discuss later, this effect is due to the new $\mathrm{BR}(B_s \to \mu^+\mu^-)$ constraint. On the other hand, the best fit in the high-mass CMSSM 'island' is more similar to the previous best fit to the $\mathrm{LHC}_{1/\mathrm{fb}}$ data set. In general terms, we see that the area of the NUHM1 $(m_0, m_{1/2})$ plane that is allowed at the 68 and 95% CL is larger than in the $(m_0, m_{1/2})$ plane of the CMSSM. This reflects the fact that the dependence of the global χ^2 function on these variables is weaker in the NUHM1 than in the CMSSM, reflecting the additional freedom offered by the degree of Higgs-mass non-universality.

In particular, the 68% CL region in the NUHM1 is connected, and extends to larger m_0 than in the CMSSM. This extension reflects the fact that in the NUHM1 a rapid-annihilation funnel region may appear at smaller $m_{1/2}$ and $\tan\beta$ than in the CMSSM for the same value of m_0, thanks to the variation in M_A that is possible in the NUHM1, allowing $M_A \sim 2m_{\tilde{\chi}_1^0}$ in different regions of the $(m_0, m_{1/2})$ plane. It is this freedom in the location of the rapid-annihilation funnel, a

[6] This could also be inferred from Figs. 7 and 9 of the paper by JE and KAO in [7].

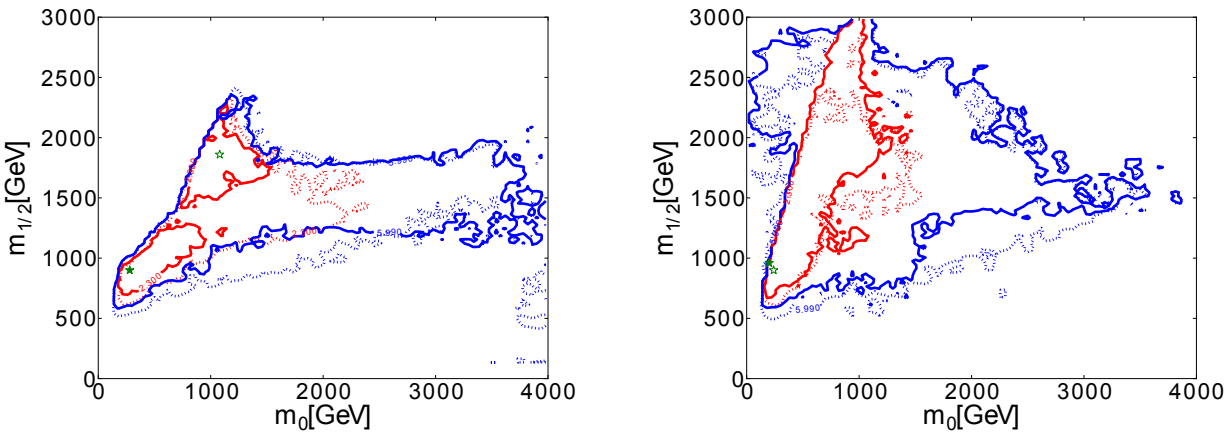

Figure 6. *The $(m_0, m_{1/2})$ planes in the CMSSM (left panel) and the NUHM1 (right panel) including the ATLAS 5/fb jets + $\not{E}_T$ constraint [12], a combination of the ATLAS [21], CDF [22], CMS [23] and LHCb [24] constraints on* BR$(B_s \to \mu^+\mu^-)$ *[25] and the recent XENON100 result [27], assuming* $M_h = 125 \pm 1$ (exp.) ± 1.5 (theo.) GeV. *The results of the current fits are indicated by solid lines and filled stars, and previous fits based on* ~ 1*/fb of LHC data are indicated by dashed lines and open stars. The blue lines denote 68% CL contours, and the red lines denote 95% CL contours.*

characteristic of the NUHM1, that is largely responsible for the expansion in the region of the $(m_0, m_{1/2})$ plane that is favoured at the 68% CL in the NUHM1, compared with the CMSSM [7].

Table 2 summarizes some interesting contributions to the global χ^2 function, namely those contributing $\Delta\chi^2 > 1$, ATLAS 5/fb jets + $\not{E}_T$ and the new global combination of BR$(B_s \to \mu^+\mu^-)$ measurements. We present their contributions at the best-fit point in the CMSSM (which has relatively high mass parameters), at the local best-fit point in the low-mass 'island' in Fig. 6, at the best-fit point in the NUHM1, and at a high-mass point in the NUHM1. We see that BR$(b \to s\gamma)$ favours lower masses in the NUHM1, whereas BR$(B_u \to \tau\nu_\tau)$ applies an essentially constant $\Delta\chi^2$ penalty [8]. None of the preferred models gives a good fit to $(g-2)_\mu$, since they reproduce approximately the SM value, though lower masses are somewhat preferred, particularly in the NUHM1. The lower-mass fits worsen the fit to M_W and that in the CMSSM (NUHM1) worsens (improves) the fit to A_ℓ(SLD), but there are only small changes in $\sigma^0_{\rm had}$. We note that the ATLAS 5/fb jets + $\not{E}_T$ constraint favours higher masses, whereas the new BR$(B_s \to \mu^+\mu^-)$ constraint favours the low-mass region in the CMSSM and (marginally) in the NUHM1, and all the models fit XENON100 equally well.

The $(\tan\beta, m_{1/2})$ *planes*

As can be seen in the left panel of Fig. 7, where the $(\tan\beta, m_{1/2})$ plane in the CMSSM is shown, the two 'islands' visible in the $(m_0, m_{1/2})$ plane of the CMSSM (left panel of Fig. 6) correspond to different ranges of $\tan\beta$. Large values of $\tan\beta \sim 45$ are favoured only at large $m_{1/2} >$ 1500 GeV, and values of $\tan\beta$ as low as ~ 10 come within the $\Delta\chi^2 = 2.30$ (68% CL) region for $m_{1/2} \sim 800$ GeV, consistent with their association with funnel and stau coannihilation regions

[7] The relic density may also be brought into the WMAP range because the $\tilde{\chi}^0_1$ acquires a relatively large higgsino component, another possibility made possible by the variation in μ that is possible in the NUHM1.

[8] We note that the Belle Collaboration has recently reported a new measurement of BR$(B_u \to \tau\nu_\tau)$ that is in better agreement with the Standard Model and the classes of supersymmetric models discussed here [56].

Model	Data set	Minimum χ^2/d.o.f.	Prob-ability	m_0 (GeV)	$m_{1/2}$ (GeV)	A_0 (GeV)	$\tan\beta$
CMSSM	$\mathrm{LHC}_{1/\mathrm{fb}}$	31.0/23	12%	1120	1870	1220	46
	$\mathrm{ATLAS}_{5/\mathrm{fb}}$ (low)	32.8/23	8.5%	300	910	1320	16
	$\mathrm{ATLAS}_{5/\mathrm{fb}}$ (high)	33.0/23	8.0%	1070	1890	1020	45
NUHM1	$\mathrm{LHC}_{1/\mathrm{fb}}$	28.9/22	15%	270	920	1730	27
	$\mathrm{ATLAS}_{5/\mathrm{fb}}$ (low)	31.3/22	9.1%	240	970	1860	16
	$\mathrm{ATLAS}_{5/\mathrm{fb}}$ (high)	31.8/22	8.1%	1010	2810	2080	39

Table 1
The best-fit points found in global CMSSM and NUHM1 fits using the ATLAS 5/fb jets + $\not{E}_T$ constraint [12], the combination of the ATLAS [21], CDF [22], CMS [23] and LHCb [24] $\mathrm{BR}(B_s \to \mu^+\mu^-)$ *[25] constraints and the updated values of M_W and m_t, compared with those found previously in global fits based on the $\mathrm{LHC}_{1/\mathrm{fb}}$ data set. In both cases, we include a measurement of $M_h = 125 \pm 1.0 \pm 1.5$ GeV and the new XENON100 constraint [27]. In the case of the CMSSM, we list the parameters of the best-fit points in both the low- and high-mass 'islands' in Fig. 6, and we quote results for a high-mass NUHM1 point as well as the low-mass best-fit point in this model. We note that the overall likelihood function is quite flat in bot the CMSSM and the NUHM1, so that the precise locations of the best-fit points are not very significant, and we do not quote uncertainties. For completeness, we note that in the best NUHM1 fit $m_H^2 \equiv m_{H_u}^2 = m_{H_d}^2 = -6.5 \times 10^6$ GeV^2, compared with -5.5×10^6 GeV^2 previously.*

respectively. We see again in the right panel of Fig. 7 that the region of the $(\tan\beta, m_{1/2})$ plane that is allowed in the NUHM1 at the 68% CL is connected, and there is no strong separation between the low- and high-mass regions. As in Fig. 6, the region of the $(\tan\beta, m_{1/2})$ plane allowed at the 95% CL is also enlarged in the NUHM1, compared to the CMSSM. The region at large $m_{1/2}$ and relatively small $\tan\beta$ corresponds to the grouping of points at low m_0 and large $m_{1/2}$ already noted in the right panel of Fig. 6.

The $(M_A, \tan\beta)$ planes

We see in the left panel of Fig. 8, where the $(M_A, \tan\beta)$ plane in the CMSSM is shown, that relatively large values of M_A are favoured in this model, $M_A > 1200$ GeV at the 68% CL and > 1000 GeV at the 95% CL. As is seen by comparing the solid contours corresponding to $\Delta\chi^2$ contours in this fit with the dotted lines corresponding to the analysis in [2], we see substantial retreats at small M_A and large $\tan\beta$ that are due to the updated $\mathrm{BR}(B_s \to \mu^+\mu^-)$ constraint. In the NUHM1, smaller values of M_A are allowed at low $\tan\beta$, as low as ~ 500 GeV at the 68% CL and ~ 350 GeV at the 95% CL. On the other hand, a substantial region of the NUHM1 $(M_A, \tan\beta)$ plane at small M_A and large $\tan\beta$ is also excluded by the new $\mathrm{BR}(B_s \to \mu^+\mu^-)$ constraint [9].

7. Relative Impacts of $\mathrm{ATLAS}_{5/\mathrm{fb}}$, $\mathrm{BR}(B_s \to \mu^+\mu^-)$ and XENON100

In this Section we analyze in more detail the different impacts of the new ATLAS 5/fb jets + $\not{E}_T$, $\mathrm{BR}(B_s \to \mu^+\mu^-)$ and XENON100 constraints on the CMSSM and NUHM1.

[9] We see in both panels of Fig. 8 'archipelagos' at large M_A that might evolve with more sampling into connected regions allowed at the 95% CL. In the NUHM1, this region is mainly populated by the points with small m_0 and large $m_{1/2}$ visible in the corresponding panel of Fig. 6.

Observable	$\Delta\chi^2$ CMSSM (high)	$\Delta\chi^2$ CMSSM (low)	$\Delta\chi^2$ NUHM1 (high)	$\Delta\chi^2$ NUHM1 (low)
Global	33.0	32.8	31.8	31.3
$\mathrm{BR}^{\mathrm{EXP/SM}}_{\mathrm{b}\to\mathrm{s}\gamma}$	1.15	1.19	0.94	0.18
$\mathrm{BR}^{\mathrm{EXP/SM}}_{\mathrm{B}\to\tau\nu}$	1.10	1.03	1.04	1.08
$a_\mu^{\mathrm{EXP}} - a_\mu^{\mathrm{SM}}$	9.69	8.48	10.47	7.82
M_W [GeV]	0.10	1.50	0.24	1.54
R_ℓ	0.95	1.09	1.09	1.12
$A_{\mathrm{fb}}(b)$	8.16	6.64	5.68	6.43
A_ℓ(SLD)	2.49	3.51	4.36	3.68
σ^0_{had}	2.58	2.50	2.55	2.50
ATLAS 5/fb jets $+\not{E}_T$	0.09	1.73	0.02	1.18
$\mathrm{BR}(B_s \to \mu^+\mu^-)$	2.52	1.22	1.59	1.70
XENON100	0.13	0.12	0.14	0.13

Table 2
Summary of the contributions of the most important observables to the global χ^2 function at the best-fit high- and low-mass points in the CMSSM and NUHM1 (those with $\Delta\chi^2 > 1$) , and of the main updated observables ATLAS 5/fb jets $+\not{E}_T$, $\mathrm{BR}(B_s \to \mu^+\mu^-)$ and XENON100.

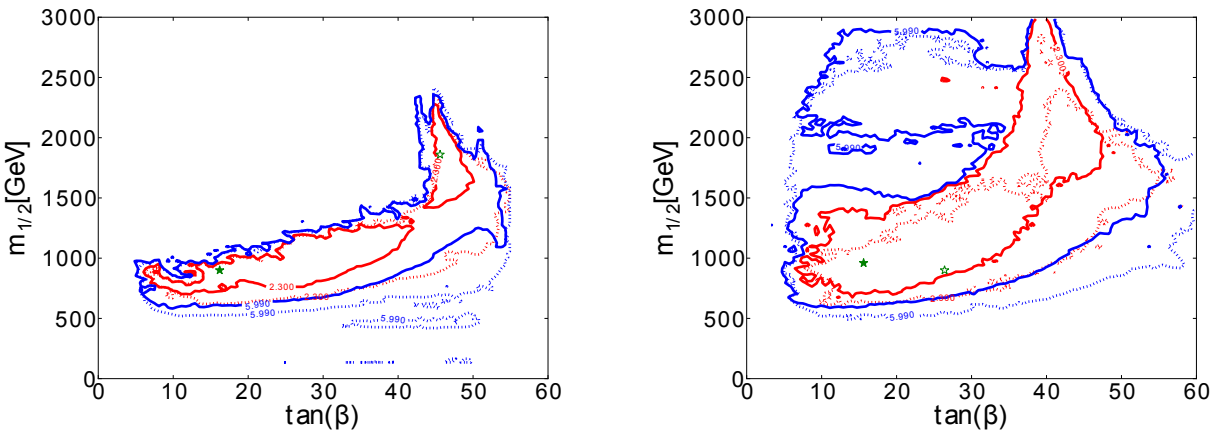

Figure 7. *The $(\tan\beta, m_{1/2})$ planes in the CMSSM (left panel) and the NUHM1 (right panel) including the ATLAS 5/fb jets $+\not{E}_T$ constraint [12], a combination of the ATLAS [21], CDF [22], CMS [23] and LHCb [24] constraints on $\mathrm{BR}(B_s \to \mu^+\mu^-)$ [25]. In both cases, we include a measurement of $M_h = 125 \pm 1.0 \pm 1.5$ GeV and the new XENON100 constraint [27]. The results of the current fits are indicated by solid lines and filled stars, and previous fits based on ~ 1/fb of LHC data are indicated by dashed lines and open stars. The blue lines denote 68% CL contours, and the red lines denote 95% CL contours.*

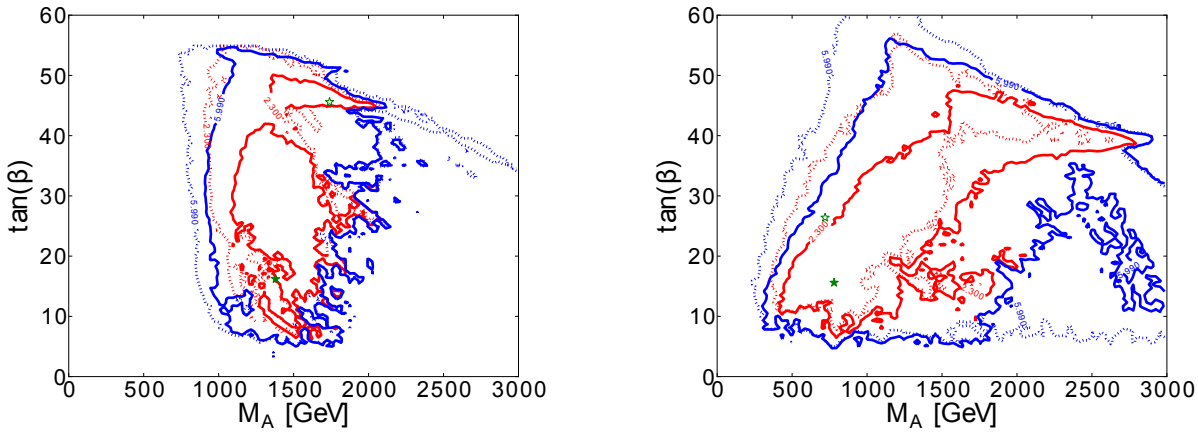

Figure 8. *The* $(M_A, \tan\beta)$ *planes in the CMSSM (left panel) and the NUHM1 (right panel) including the ATLAS 5/fb jets* $+\not{E}_T$ *constraint, a combination of the ATLAS, CDF, CMS and LHCb constraints on* $\mathrm{BR}(B_s \to \mu^+\mu^-)$*. In both cases, we include a measurement of* $M_h = 125 \pm 1.0 \pm 1.5$ GeV *and the new XENON100 constraint [27]. The results of the current fits are indicated by solid lines and filled stars, and previous fits based on* ~ 1*/fb of LHC data are indicated by dashed lines and open stars. The blue lines denote 68% CL contours, and the red lines denote 95% CL contours.*

Fig. 9 displays the impacts in the $(m_0, m_{1/2})$ planes of the CMSSM (left panels) and the NUHM1 (right panels) of dropping the ATLAS 5/fb jets $+\not{E}_T$ constraint (top panels), the new $\mathrm{BR}(B_s \to \mu^+\mu^-)$ constraint (middle panels), or the new XENON100 constraint (bottom panels). In each panel, we compare the 68 and 95% CL contours in the full global fit (dashed lines) with a fit dropping one of the constraints (solid lines). The corresponding best fit points are shown as open and closed stars.

In the CMSSM case, very little effect is seen when the ATLAS 5/fb jets $+\not{E}_T$ constraint is dropped. On the other hand, when $\mathrm{BR}(B_s \to \mu^+\mu^-)$ is dropped there are significant extensions of the 68 and 95% CL regions: the two 68% CL 'islands' at low m_0 merge and extend to larger m_0, and the 95% band extending to large m_0 broadens to a much larger range of $m_{1/2}$. When the new XENON100 constraint is dropped, the main effect is the appearance of the focus-point region at large m_0 and small $m_{1/2}$.

In the NUHM1 case, dropping the ATLAS 5/fb jets $+\not{E}_T$ constraint again has little effect on the contours, except at small m_0 and $m_{1/2}$. Dropping the $\mathrm{BR}(B_s \to \mu^+\mu^-)$ constraint has more effect on the 68 and 95% CL contours in the NUHM1. The effect of dropping the new XENON100 constraint is qualitatively similar to that of dropping the new $\mathrm{BR}(B_s \to \mu^+\mu^-)$ constraint, except that it allows a larger region at small $m_{1/2}$ and large m_0.

Similarly, Fig. 10 displays the impacts in the $(M_A, \tan\beta)$ planes of the CMSSM (left) panels and the NUHM1 (right panels) of dropping the ATLAS 5/fb jets $+\not{E}_T$ constraint (top panels), the new $\mathrm{BR}(B_s \to \mu^+\mu^-)$ constraint (middle panels) or the new XENON100 constraint (bottom panels). As in the $(m_0, m_{1/2})$ planes, we see relatively little impact in either the CMSSM or the NUHM1 from dropping the ATLAS 5/fb jets $+\not{E}_T$ constraint, and a much bigger effect from dropping the new $\mathrm{BR}(B_s \to \mu^+\mu^-)$ constraint, particularly at small M_A and large $\tan\beta$. In both cases, the $\mathrm{BR}(B_s \to \mu^+\mu^-)$ constraint reduces drastically the value of $\tan\beta$ at the best-fit point from $\sim 46(27)$ in the CMSSM (NUHM1) to ~ 16. On the other hand, most of the impact of drop-

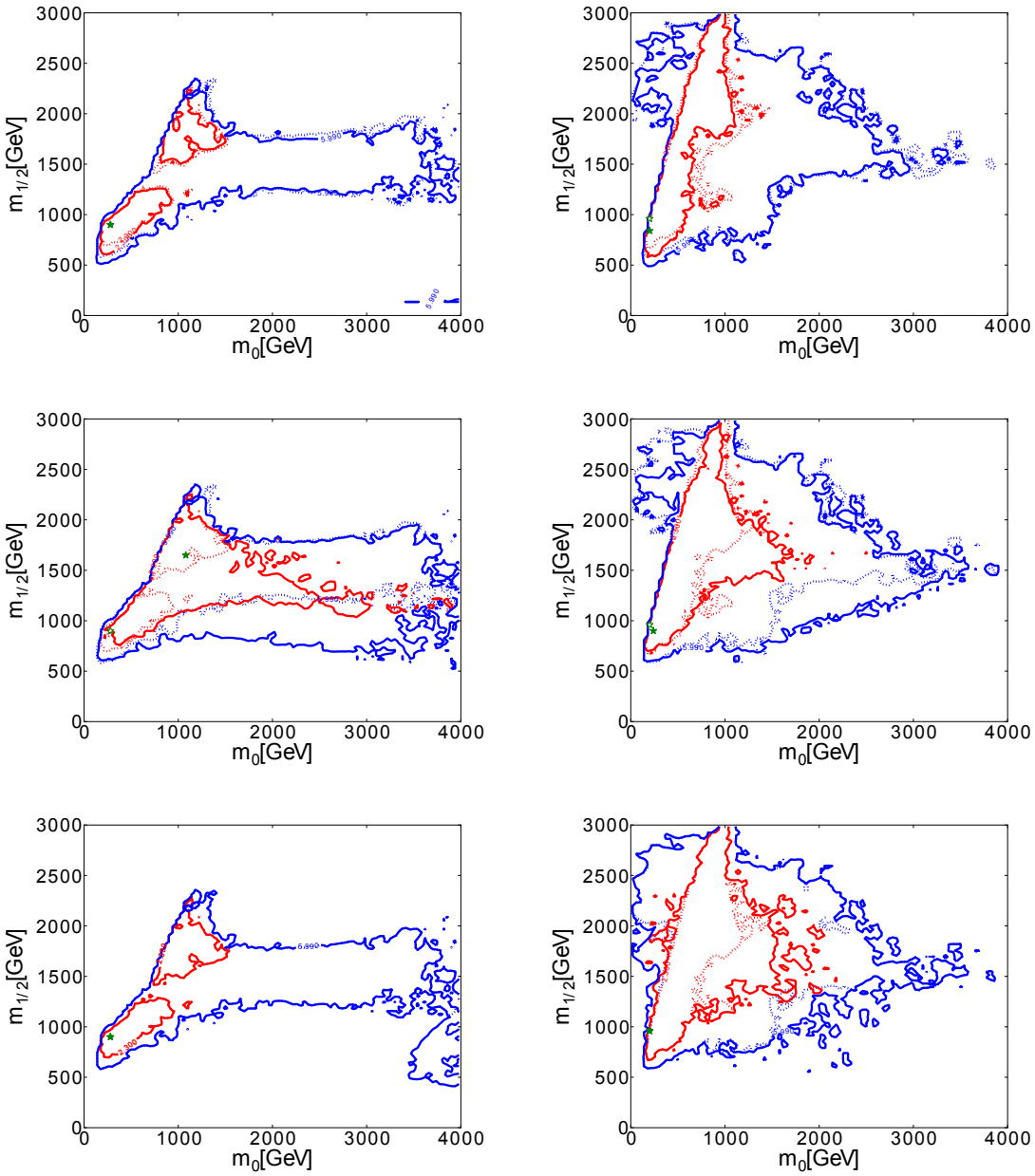

Figure 9. *The $(m_0, m_{1/2})$ planes in the CMSSM (left panels) and the NUHM1 (right panels) displaying the effects of dropping the ATLAS 5/fb jets + $\not{E}_T$ constraint (top panels), the new* $\mathrm{BR}(B_s \to \mu^+\mu^-)$ *constraint (middle panels) and the new XENON100 constraint (bottom panels). In each case, the full global fit is represented by an open green star and dashed blue and red lines for the 68 and 95% CL contours, whilst the fits to the incomplete data sets are represented by closed stars and solid contours.*

ping the new XENON100 constraint is to expand the preferred region at large M_A and $tb < 40$.

We analyse the various χ^2 contributions and best-fit points in more detail in Table 3. Here we display the principal changes in the best-fit parameters from the new global fit (second column) when dropping the $\text{ATLAS}_{5/\text{fb}}$ constraint (third column), dropping the new $\text{BR}(B_s \to \mu^+\mu^-)$ constraint (fourth column), dropping the new XENON100 constraint (fifth column), and dropping all three new constraints, i.e., the analysis of [2] (last column). We see that it is $\text{BR}(B_s \to \mu^+\mu^-)$ that, among the new constraints, has the most significant impact on the best-fit parameters of the NUHM1, principally $\tan\beta$. In the lower rows we show the χ^2 contributions of the direct SUSY searches, denoted as $\Delta\chi^2$ for $\not{E}_T$, $\text{BR}(B_s \to \mu^+\mu^-)$ and $(g-2)_\mu$. One can clearly observe that the contribution of $(g-2)_\mu$ to the total χ^2 function increases when $\text{BR}(B_s \to \mu^+\mu^-)$ and the other new constraints are incorporated, demonstrating once again that the new data are pushing simple supersymmetry-breaking models such as the NUHM1 (and CMSSM) out of the 'sweet spot' where the experimental measurement of $(g-2)_\mu$ could easily be explained.

8. Predictions for Physical Observables

In this section we present one-dimensional χ^2 likelihood functions for slected physical observables, based on the above surveys of the CMSSM and NUHM1 parameter spaces, comparing results based on the $\text{LHC}_{1/\text{fb}}$ and $\text{LHC}_{5/\text{fb}}$ data sets.

The Gluino Mass

Fig. 11 displays the χ^2 functions for $m_{\tilde{g}}$ in the CMSSM (left panel) and the NUHM1 (right panel), for fits to the $\text{LHC}_{5/\text{fb}}$ data including the new $\text{BR}(B_s \to \mu^+\mu^-)$ and XENON100 limits (solid lines) and to the $\text{LHC}_{1/\text{fb}}$ data including the $\text{BR}(B_s \to \mu^+\mu^-)$ limits then available (dashed lines). In the case of the CMSSM, we see a bimodal distribution, with local minima at $m_{\tilde{g}} \sim 2000$ GeV and ~ 4000 GeV, corresponding to the best fits in the low- and high-mass islands discussed above, whose values of χ^2 are almost indistinguishable. Intermediate values of $m_{\tilde{g}}$ are disfavoured by $\Delta\chi^2 \lesssim 2$, though the envelope of the χ^2 function could only be reduced by further sampling. In the case of the NUHM1, a much more weakly bimodal distribution is visible. In the CMSSM, values of $m_{\tilde{g}}$ between ~ 1500 GeV and ~ 4800 GeV are allowed at the $\Delta\chi^2 < 2$ level, and in the NUHM1 values over 6000 GeV are allowed at this level. Once again, the ability to move to large masses (in this case the gluino mass or $m_{1/2}$) can be traced to the freedom in the NUHM1 of adjusting $M_A \sim 2m_\chi$ so that the relic density is at the WMAP value. At such large masses, there is essentially no further price paid by $g_\mu - 2$ or other low energy observables as we approach the decoupling limit.

The Squark Mass

Fig. 12 displays the χ^2 functions for the average mass of the supersymmetric partners of the five lightest right-handed quarks, $m_{\tilde{q}}$, in the CMSSM (left panel) and the NUHM1 (right panel), for fits to the $\text{LHC}_{5/\text{fb}}$, $\text{BR}(B_s \to \mu^+\mu^-)$ and new XENON100 data (solid lines) and the $\text{LHC}_{1/\text{fb}}$ data (dashed lines), as in Fig. 11. In the case of the CMSSM, we see local minima of χ^2 at $m_{\tilde{q}} \sim$ 1800 and 3500 GeV, separated again by a range with $\Delta\chi^2 \lesssim 2$. At this level of $\Delta\chi^2$, any value of $m_{\tilde{q}}$ between ~ 1200 GeV and ~ 4200 GeV is allowed. In the case of the NUHM1, there is a similar structure, but it is less pronounced and the intermediate range has $\Delta\chi^2 \sim 1$. Only squark mass values above ~ 5.4 TeV receive a substantial χ^2 penalty, which is due to large m_0 being disfavoured in this model.

The Stop Mass

Fig. 13 displays the χ^2 functions for the lighter stop squark mass $m_{\tilde{t}_1}$ in the CMSSM (left panel) and the NUHM1 (right panel), for fits to the $\text{LHC}_{5/\text{fb}}$, $\text{BR}(B_s \to \mu^+\mu^-)$ and new XENON100 data set (solid lines) and the $\text{LHC}_{1/\text{fb}}$ data (dashed lines), as in Fig. 11. We see that the CMSSM χ^2 is minimized for $m_{\tilde{t}_1} \sim 1100$ GeV, with a secondary minimum for $m_{\tilde{t}_1} \sim 2900$ GeV, whereas in the NUHM1 χ^2 is minimized for $m_{\tilde{t}_1} \sim$ 1700 GeV with values above around 4.5 TeV being disfavoured. In both models, values of $m_{\tilde{t}_1} < m_{\tilde{q}}$ are expected.

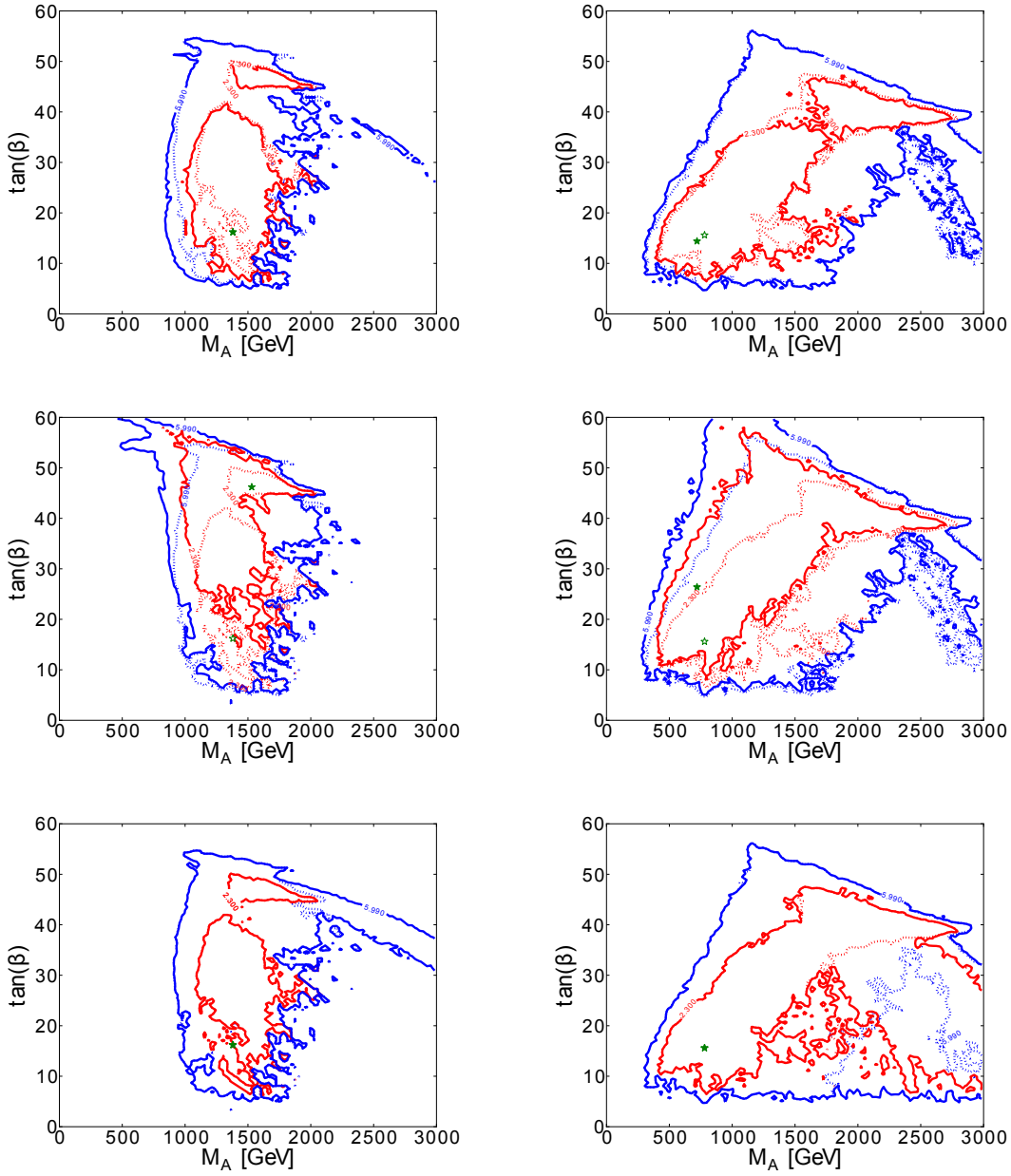

Figure 10. *The* $(M_A, \tan\beta)$ *planes in the CMSSM (left panels) and the NUHM1 (right panels) displaying the effects of dropping the ATLAS 5/fb jets* $+ \not{E}_T$ *constraint (top panels), the new* $\mathrm{BR}(B_s \to \mu^+\mu^-)$ *constraint (middle panels) or the new XENON100 constraint (bottom panels). In each case, the full global fit is represented by an open green star and dashed blue and red lines for the 68 and 95% CL contours, whilst the fits to the incomplete data sets are represented by closed stars and solid contours.*

Quantity	Full fit	w/o ATLAS$_{5/\mathrm{fb}}$	w/o $B_s \to \mu^+\mu^-$	w/o XENON100	LHC$_{1/\mathrm{fb}}$ fit
Total χ^2	31.3	30.1	28.7	31.3	28.9
m_0 (GeV)	240	240	270	240	270
$m_{1/2}$ (GeV)	970	870	920	970	920
A_0 (GeV)	1860	1860	1730	1860	1730
$\tan\beta$	16	15	27	16	27
m_H^2 (GeV^2)	-6.5×10^6	-5.6×10^6	-5.5×10^6	-6.5×10^6	-5.5×10^6
$\Delta\chi^2$ $\not{E}_T$	1.18	1.06*	1.36	1.18	0.85*
$\Delta\chi^2$ $B_s \to \mu^+\mu^-$	1.70	1.12	0.21*	1.70	0.21*
$\Delta\chi^2$ XENON100	0.13	0.13	0.13	0.14*	0.14*
$\Delta\chi^2$ $(g-2)_\mu$	7.82	7.41	5.99	7.82	5.99

Table 3

Principal changes in the best-fit parameters in the NUHM1 from the new global fit (second column) when dropping the ATLAS$_{5/\mathrm{fb}}$ constraint (third column), dropping the new BR($B_s \to \mu^+\mu^-$) *constraint (fourth column), dropping the new XENON100 constraint (fifth column) and dropping all three new constraints, i.e., the analysis of [2] (last column). The bottom four lines display the contributions to χ^2 of the $\not{E}_T$,* BR($B_s \to \mu^+\mu^-$)*, XENON100 and $(g-2)_\mu$ constraints. The numbers marked by * are for the implementations of these constraints in [2].*

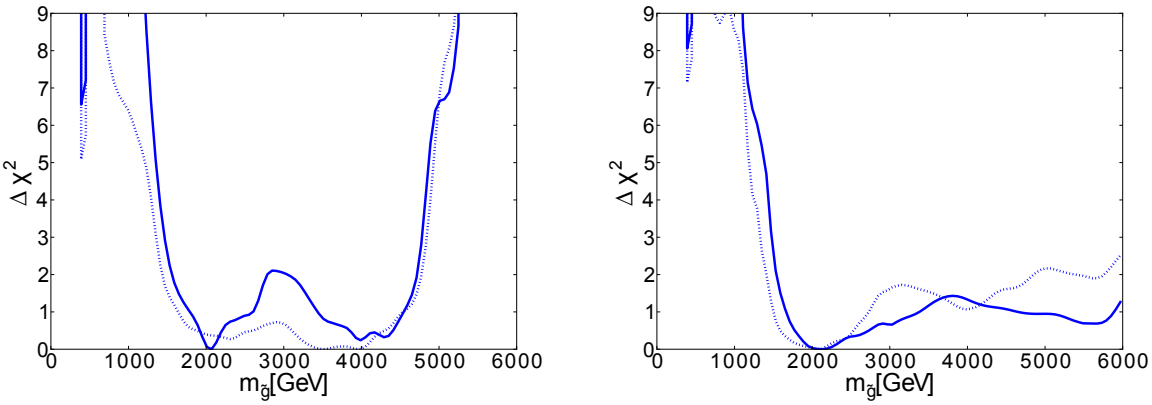

Figure 11. *The χ^2 likelihoods in the CMSSM (left panel) and NUHM1 (right panel) as functions of $m_{\tilde{g}}$ based on global fits to the LHC$_{5/\mathrm{fb}}$,* BR($B_s \to \mu^+\mu^-$) *and new XENON100 data set (solid lines), and to the LHC$_{1/\mathrm{fb}}$ data set (dashed lines).*

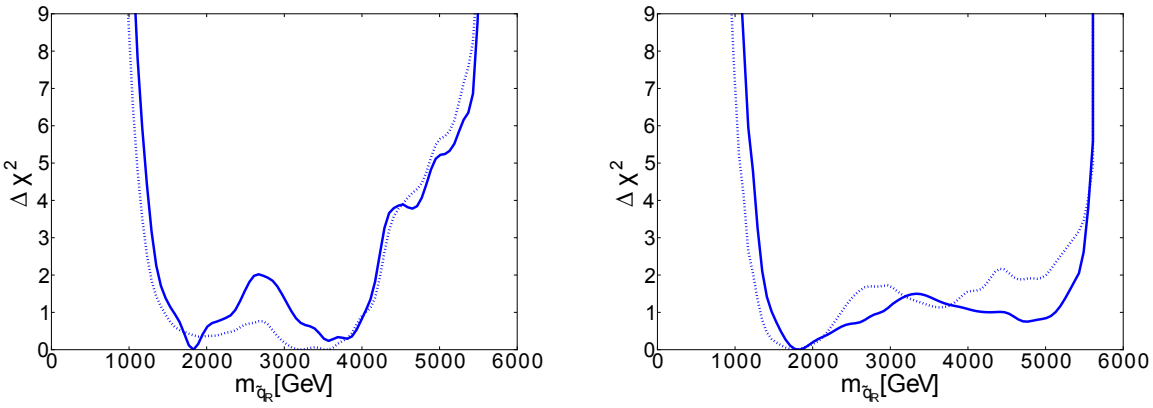

Figure 12. *The χ^2 likelihoods in the CMSSM (left panel) and NUHM1 (right panel) as functions of $m_{\tilde{q}}$ based on global fits to the LHC$_{5/\mathrm{fb}}$, BR($B_s \to \mu^+\mu^-$) and new XENON100 data set (solid lines), and to the LHC$_{1/\mathrm{fb}}$ data set (dashed lines).*

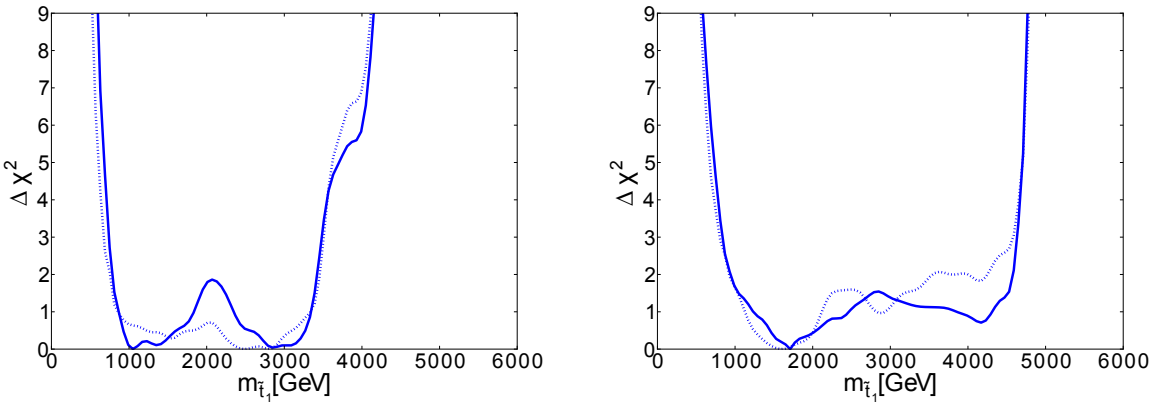

Figure 13. *The χ^2 likelihoods in the CMSSM (left panel) and NUHM1 (right panel) as functions of $m_{\tilde{t}_1}$ based on global fits to the LHC$_{5/\mathrm{fb}}$, BR($B_s \to \mu^+\mu^-$) and new XENON100 data set (solid lines), and to the LHC$_{1/\mathrm{fb}}$ data set (dashed lines).*

The Stau Mass

Likewise, Fig. 14 displays the χ^2 functions for $m_{\tilde{\tau}_1}$ in the CMSSM (left panel) and the NUHM1 (right panel), for fits to the LHC$_{5/\mathrm{fb}}$, BR($B_s \to \mu^+\mu^-$) and new XENON100 data set (solid lines) and the LHC$_{1/\mathrm{fb}}$ data (dashed lines), as in Fig. 11. In this case, in the CMSSM χ^2 is minimized for $m_{\tilde{\tau}_1} \sim 400$ and ~ 800 GeV, whereas in the NUHM1 χ^2 is minimized for $m_{\tilde{\tau}_1} \sim 700$ GeV with an upper limit around 2.5 TeV.

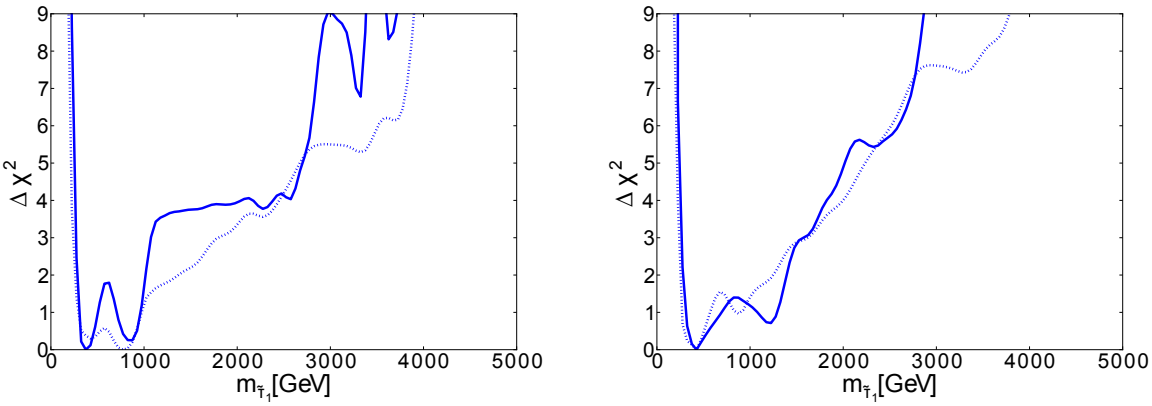

Figure 14. *The χ^2 likelihoods in the CMSSM (left panel) and NUHM1 (right panel) as functions of $m_{\tilde{\tau}_1}$ based on global fits to the LHC$_{5/\mathrm{fb}}$, BR($B_s \to \mu^+\mu^-$) and new XENON100 data set (solid lines), and to the LHC$_{1/\mathrm{fb}}$ data set (dashed lines).*

The Higgs Mass

In Fig. 15 we show as solid lines the χ^2 functions for M_h in the CMSSM (left panel) and the NUHM1 (right panel), for fits to the LHC$_{5/\mathrm{fb}}$, BR($B_s \to \mu^+\mu^-$) and new XENON100 data set, but *omitting* all the direct constraints on the Higgs mass from the LHC, LEP and Tevatron. Thus, Fig. 15 displays the predictions for M_h in the CMSSM and NUHM1 on the basis of the other constraints. As in previous publications (see [1, 2, 14] and references therein), the plots in Fig. 15 include a red band with a width of 1.5 GeV to represent the theoretical uncertainty. These plots show *directly* the extent to which the indirect prediction of M_h agrees with the (provisional) direct measurement. Also shown in Fig. 15 is the LEP exclusion for a SM Higgs boson (shaded yellow), and the range indicated by the LHC discovery (shaded green). We see that the LHC measurement of M_h is somewhat larger than would be indicated by our best fit based on other data, but not disastrously so, with $\Delta\chi^2 \sim 1.5$ in the CMSSM and ~ 0.5 in the NUHM1.

BR($B_s \to \mu^+\mu^-$)

Fig. 16 displays the χ^2 functions for BR($B_s \to \mu^+\mu^-$) in the CMSSM (left panel) and the NUHM1 (right panel), for fits to the LHC$_{5/\mathrm{fb}}$, BR($B_s \to \mu^+\mu^-$) and new XENON100 data set (solid lines) and the LHC$_{1/\mathrm{fb}}$ data (dashed lines), as in Fig. 11. Comparing the solid and dotted lines, we see the strong impact of the recent BR($B_s \to \mu^+\mu^-$) update. In both the CMSSM and the NUHM1, values of BR($B_s \to \mu^+\mu^-$) above the SM value are preferred over values below the SM value. We see that, in either case, a measurement of BR($B_s \to \mu^+\mu^-$) at the level of 30%, which may soon be possible, would greatly restrict the preferred ranges of both the CMSSM and NUHM1 parameter spaces.

σ_p^{SI}

Fig. 17 displays the best-fit points and the 68% and 95% CL contours (red and blue, respectively) in the $(m_{\tilde{\chi}_1^0}, \sigma_p^{\mathrm{SI}})$ planes in the CMSSM (left panel) and and the NUHM1 (right panel). The solid lines are for the global fit to the LHC$_{5/\mathrm{fb}}$ BR($B_s \to \mu^+\mu^-$) and new XENON100 data set, and the dashed lines for the previous LHC$_{1/\mathrm{fb}}$ fit, and the solid (open) green stars mark the corresponding best-fit points [10]. We see that the region

[10] We display results for $m_{\tilde{\chi}_1^0} \leq 1$ TeV only, because results from XENON100 are not published for larger masses.

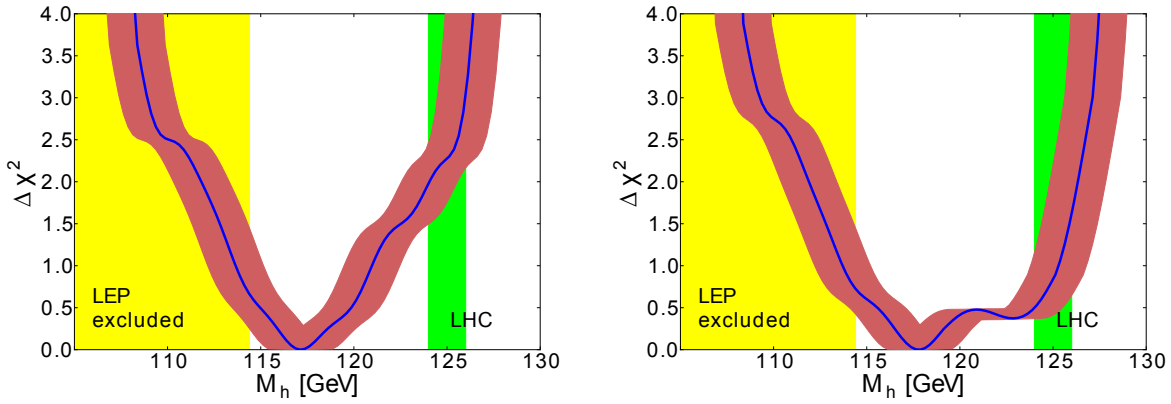

Figure 15. *The one-dimensional* $\Delta\chi^2$ *functions for* M_h *in the CMSSM (left) and the NUHM1 (right). The solid lines are for fits including all the available data including* $(g-2)_\mu$ *but excluding the direct LEP [61, 62], Tevatron [?] and LHC [36, 37] constraints on* M_h*, with a red band indicating the estimated theoretical uncertainty in the calculation of* M_h *of* ~ 1.5 GeV*. The shaded ranges are those excluded by LEP searches for a SM Higgs boson (yellow) and indicated by the LHC discovery (green).*

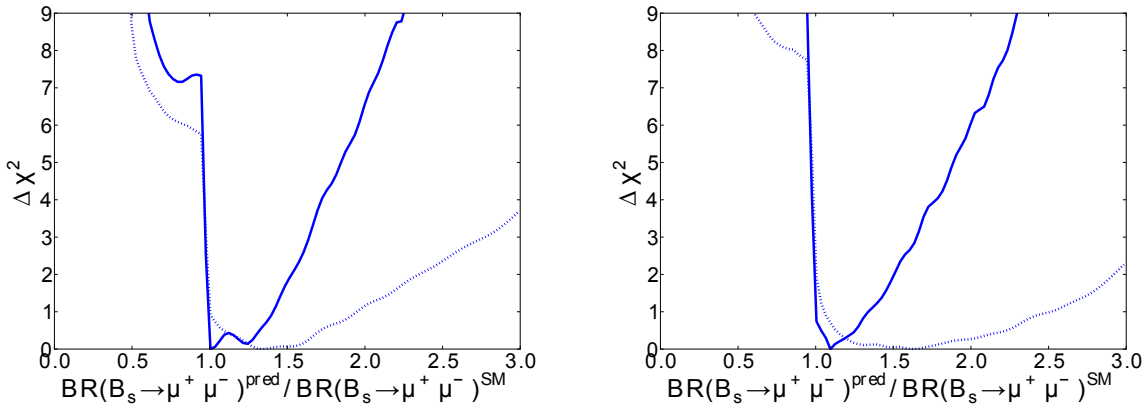

Figure 16. *The* χ^2 *likelihoods in the CMSSM (left panel) and NUHM1 (right panel) as functions of* $\mathrm{BR}(B_s \to \mu^+\mu^-)$ *based on global fits to the* $LHC_{5/\mathrm{fb}}$*,* $\mathrm{BR}(B_s \to \mu^+\mu^-)$ *and new XENON100 data set (solid lines), and to the* $LHC_{1/\mathrm{fb}}$ *data set (dashed lines).*

of the $(m_{\tilde{\chi}_1^0}, \sigma_p^{\mathrm{SI}})$ favoured in the CMSSM is now more restricted, in particular at small $m_{\tilde{\chi}_1^0}$. The main effect of the new XENON100 constraint has been to remove focus points with large σ_p^{SI} that were previously allowed at the 95% CL.

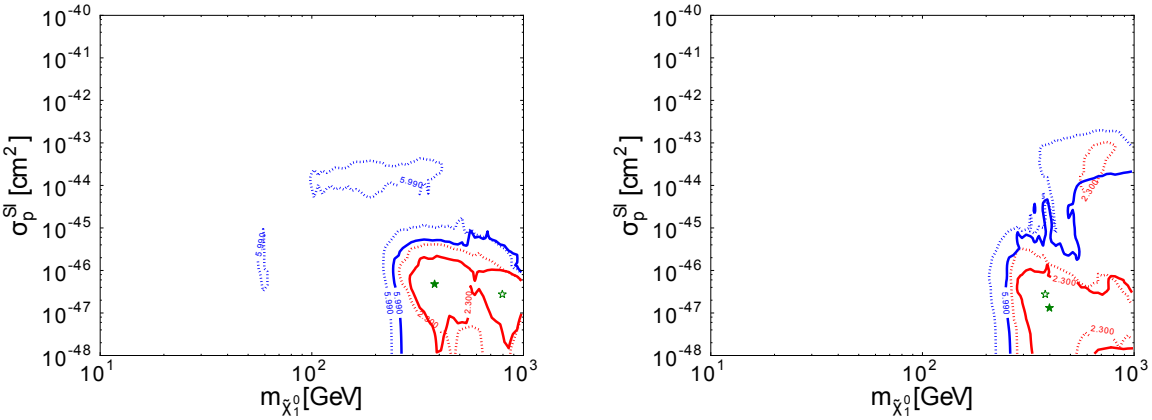

Figure 17. *The* $(m_{\tilde{\chi}_1^0}, \sigma_p^{\rm SI})$ *planes in the CMSSM (left panel) and the NUHM1 (right panel). The* $\Delta\chi^2 = 2.30(5.99)$ *contours, corresponding to the 68(95)% CL are coloured red (blue). The solid (dashed) lines are for global fits to the* $LHC_{5/\rm fb}$, $\mathrm{BR}(B_s \to \mu^+\mu^-)$ *and new XENON100 (*$LHC_{1/\rm fb}$*) data, and the corresponding best-fit points are indicated by solid (open) green stars.*

9. Comparison with other Analyses

We are not aware of any global analyses incorporating the new XENON100 constraint [27]. The two global analyses including LHC 5/fb data that are most similar to ours are [9] and [10], and we take this opportunity to comment on the relations and differences between those and the present work.

As in this work, Ref. [9] incorporates the constraints imposed by the $\mathrm{LHC}_{5/\rm fb}$ data using an implementation of `Delphes` that is reported to reproduce the 95% CL limits published previously by ATLAS using 165/pb and 1/fb of data and shown to reproduce approximately the 95% CL limits for $\tan\beta = 10$ and A_0 found in the ATLAS analysis used here and the CMS razor analyss with 5/fb of data [13]. However, the ATLAS 5/fb jets + $\not{E}_T$ analysis has apparently not been modelled in detail, and full information is not available on its validation for other values of the CMSSM parameters, nor on its extension to the NUHM1. In contrast to previous papers by the same collaboration that used the `MasterCode`, Ref. [9] uses only a reduced set of precision electroweak and flavour observables, a topic we comment on below. In contrast, Ref. [9] uses `AstroFit`, which provides input from both direct and indirect dark matter searches, whereas we use only the direct XENON100 search. However, Ref. [9] finds that the indirect dark matter searches have negligible impact at the present time. When the constraint $M_h = 126 \pm 2 \pm 3$ GeV is imposed in [9], the results for the CMSSM are relatively similar to ours, whereas the results for the NUHM1 are only qualitatively similar.

Ref. [10] implements the CMS razor analysis using 5/fb of data, and provides more details of its efficiency and likelihood maps, and also compares with the 95% CL limit obtained in the ATLAS 5/fb jets + $\not{E}_T$ analysis. This paper favours values of the CMSSM mass parameters $(m_0, m_{1/2})$ that are considerably larger than in our analysis and in [9]. However, Ref. [10] does favour the stau coannihilation strip and the rapid-annihilation funnel regions of the CMSSM, disfavouring the focus-point region that had been advocated in previous fits by the same group. Ref. [10] does not discuss the NUHM1, but does consider the possibilities that $\mu < 0$ and of dropping the $(g-2)_\mu$ constraint.

10. Conclusions

We have presented in this paper new global fits to the CMSSM and NUHM1 based on the 7 TeV ATLAS 5/fb jets + $\not{E}_T$ constraint and the latest global combination of limits on BR($B_s \to \mu^+\mu^-$), the new XENON100 constraint, a Higgs mass measurement $M_h \sim 125$ GeV, and minor updates for other observables. Before the advent of the LHC, low-energy data, in particular $(g-2)_\mu$, gave hope that the scales of supersymmetry breaking in these models might be within reach of the LHC within its first year of operation at 7 TeV in the centre of mass. This has not been the case, and the p-values of the CMSSM and NUHM1 have declined to 8.5 and 9.1%, respectively, prompting a re-evaluation of their status.

Two possibilities remain open at this point: either supersymmetry is relatively light but manifests itself differently from the CMSSM or NUHM1, or the supersymmetry-breaking mass scale is heavier, possibly even beyond the reach of the LHC. In the first case, several possibilities suggest themselves (see, e.g., Ref. [63]): other models of supersymmetry breaking, light third-generation squarks, $\mathcal{F}$-SU(5) [11], the pMSSM, R-violating models, etc., and a discussion of these possibilities lies beyond the scope of this work. As for the second case, the global fits presented here in the CMSSM and NUHM1 give limited guidance on the possible supersymmetric mass scale.

Perhaps surprisingly, the ATLAS 5/fb jets + $\not{E}_T$ data are not much more problematic for the CMSSM and the NUHM1 than were the $\text{LHC}_{1/\text{fb}}$ data in combination with the Higgs mass constraint. The latter two had already constrained the CMSSM and NUHM1 parameters to lie beyond the range where they could fully 'solve' the $(g-2)_\mu$ problem, and the contribution of the ATLAS 5/fb jets + $\not{E}_T$ constraint to the global χ^2 function is not large, even at the local best-fit point within the low-mass CMSSM 'island'. A new feature of this analysis is the impact of the latest BR($B_s \to \mu^+\mu^-$) constraint, and we stress the importance of the constraint from the search for spin-independent dark matter scattering by the XENON100 Collaboration [27].

The most important upper limit on the supersymmetry-breaking mass scales in the CMSSM and the NUHM1 is now provided by the cold dark matter density constraint, and indications on the possible sparticle masses within the range allowed by this constraint are now quite weak. The $(g-2)_\mu$ constraint still offers some preference for low sparticle masses, but this is largely counterbalanced by other constraints such as BR($B_s \to \mu^+\mu^-$). As we have seen, any value of $m_{\tilde{g}} \in (1500, 5000)$ GeV is allowed at the $\Delta\chi^2 < 2$ level. The lower part of this range may be explored with LHC operating at 8 TeV, and the middle part with the LHC at 13 or 14 TeV, but the upper part of the allowed range of $m_{\tilde{g}}$ would lie beyond the reach of the LHC.

On the other hand, one must keep in mind that the increasing tension within the CMSSM and NUHM1 between the low-energy data, mainly $(g-2)_\mu$ and the $\text{LHC}_{5/\text{fb}}$ and BR($B_s \to \mu^+\mu^-$) data on the other side, has resulted over time in a monotonously-increasing χ^2 and a correspondingly lower fit probability. Consequently, looking beyond the CMSSM and NUHM1, to models with a different connection between the coloured and uncoloured sector, not only seems timely now, but mandatory. We expect that some model with such a different connection will give a substantially better fit to *all* existing experimental data and present more favorable expectations for subsequent LHC runs or a future LC.

Acknowledgements

The work of O.B., M.C., J.E., J.M., S.N., K.A.O. and K.J.de V. is supported in part by the London Centre for Terauniverse Studies (LCTS), using funding from the European Research Council via the Advanced Investigator Grant 267352. The work of S.H. is supported in part by CICYT (grant FPA 2010–22163-C02-01) and by the Spanish MICINN's Consolider-Ingenio 2010 Program under grant MultiDark CSD2009-00064. The work of K.A.O. is supported in part by DOE grant DE-FG02-94ER-40823 at the University of Minnesota. We thank Robert Fleischer for discussions.

REFERENCES

1. O. Buchmueller, *et al.*, Eur. Phys. J. C **72** (2012) 1878 [arXiv:1110.3568 [hep-ph]].
2. O. Buchmueller, *et al.*, Eur. Phys. J. C **72** (2012) 2020 [arXiv:1112.3564 [hep-ph]].
3. For a sampling of other post-LHC analyses, see: P. Bechtle *et al.*, arXiv:1102.4693 [hep-ph]; M. Farina, M. Kadastik, D. Pappadopulo, J. Pata, M. Raidal and A. Strumia, Nucl. Phys. B **853**, 607 (2011) [arXiv:1104.3572 [hep-ph]]; M. Baak, M. Goebel, J. Haller, A. Hoecker, D. Ludwig, K. Moenig, M. Schott and J. Stelzer, Eur. Phys. J. C **72**, 2003 (2012) [arXiv:1107.0975 [hep-ph]]; N. Bhattacharyya, A. Choudhury and A. Datta, Phys. Rev. D **84**, 095006 (2011) [arXiv:1107.1997 [hep-ph]]; A. Fowlie, A. Kalinowski, M. Kazana, L. Roszkowski and Y. L. S. Tsai, Phys. Rev. D **85**, 075012 (2012) [arXiv:1111.6098 [hep-ph]]; T. J. LeCompte and S. P. Martin, Phys. Rev. D **85**, 035023 (2012) [arXiv:1111.6897 [hep-ph]]; L. Roszkowski, E. M. Sessolo and Y. -L. S. Tsai, arXiv:1202.1503 [hep-ph].
4. H. P. Nilles, Phys. Rep. **110** (1984) 1; H. E. Haber and G. L. Kane, Phys. Rept. **117** (1985) 75.
5. M. Drees and M. M. Nojiri, Phys. Rev. D **47** (1993) 376 [arXiv:hep-ph/9207234]; G. L. Kane, C. F. Kolda, L. Roszkowski and J. D. Wells, Phys. Rev. D **49** (1994) 6173 [arXiv:hep-ph/9312272]; H. Baer and M. Brhlik, Phys. Rev. D **53** (1996) 597 [arXiv:hep-ph/9508321]; Phys. Rev. D **57** (1998) 567 [arXiv:hep-ph/9706509]; J. R. Ellis, T. Falk, K. A. Olive and M. Schmitt, Phys. Lett. B **388** (1996) 97 [arXiv:hep-ph/9607292]; Phys. Lett. B **413** (1997) 355 [arXiv:hep-ph/9705444]; J. R. Ellis, T. Falk, G. Ganis, K. A. Olive and M. Schmitt, Phys. Rev. D **58** (1998) 095002 [arXiv:hep-ph/9801445]; V. D. Barger and C. Kao, Phys. Rev. D **57** (1998) 3131 [arXiv:hep-ph/9704403]; J. R. Ellis, T. Falk, G. Ganis and K. A. Olive, Phys. Rev. D **62** (2000) 075010 [arXiv:hep-ph/0004169]; H. Baer, M. Brhlik, M. A. Diaz, J. Ferrandis, P. Mercadante, P. Quintana and X. Tata, Phys. Rev. D **63** (2001) 015007 [arXiv:hep-ph/0005027]; J. R. Ellis, T. Falk, G. Ganis, K. A. Olive and M. Srednicki, Phys. Lett. B **510** (2001) 236 [arXiv:hep-ph/0102098]; V. D. Barger and C. Kao, Phys. Lett. B **518** (2001) 117 [arXiv:hep-ph/0106189]; L. Roszkowski, R. Ruiz de Austri and T. Nihei, JHEP **0108** (2001) 024 [arXiv:hep-ph/0106334]; A. Djouadi, M. Drees and J. L. Kneur, JHEP **0108** (2001) 055 [arXiv:hep-ph/0107316]; U. Chattopadhyay, A. Corsetti and P. Nath, Phys. Rev. D **66** (2002) 035003 [arXiv:hep-ph/0201001]; J. R. Ellis, K. A. Olive and Y. Santoso, New Jour. Phys. **4** (2002) 32 [arXiv:hep-ph/0202110]; H. Baer, C. Balazs, A. Belyaev, J. K. Mizukoshi, X. Tata and Y. Wang, JHEP **0207** (2002) 050 [arXiv:hep-ph/0205325]; R. Arnowitt and B. Dutta, arXiv:hep-ph/0211417; J. R. Ellis, K. A. Olive, Y. Santoso and V. C. Spanos, Phys. Lett. B **565** (2003) 176 [arXiv:hep-ph/0303043]; H. Baer and C. Balazs, JCAP **0305**, 006 (2003) [arXiv:hep-ph/0303114]; A. B. Lahanas and D. V. Nanopoulos, Phys. Lett. B **568**, 55 (2003) [arXiv:hep-ph/0303130]; U. Chattopadhyay, A. Corsetti and P. Nath, Phys. Rev. D **68**, 035005 (2003) [arXiv:hep-ph/0303201]; C. Munoz, Int. J. Mod. Phys. A **19**, 3093 (2004) [arXiv:hep-ph/0309346]; R. Arnowitt, B. Dutta and B. Hu, arXiv:hep-ph/0310103. J. Ellis and K. A. Olive, in "Particle Dark Matter", ed. G. Bertone, pp142-163 [arXiv:1001.3651 [astro-ph.CO]].
6. H. Baer, A. Mustafayev, S. Profumo, A. Belyaev and X. Tata, Phys. Rev. D **71** (2005) 095008 [arXiv:hep-ph/0412059]; H. Baer, A. Mustafayev, S. Profumo, A. Belyaev and X. Tata, *JHEP* **0507** (2005) 065, hep-ph/0504001; J. R. Ellis, K. A. Olive and P. Sandick, Phys. Rev. D **78** (2008) 075012 [arXiv:0805.2343 [hep-ph]].
7. H. Baer, V. Barger and A. Mustafayev, Phys. Rev. D **85**, 075010 (2012) [arXiv:1112.3017 [hep-ph]]; J. L. Feng, K. T. Matchev and D. Sanford, Phys. Rev. D **85**, 075007 (2012) [arXiv:1112.3021 [hep-ph]]; T. Li,

J. A. Maxin, D. V. Nanopoulos and J. W. Walker, Phys. Lett. B **710** (2012) 207 [arXiv:1112.3024 [hep-ph]]; S. Heinemeyer, O. Stal and G. Weiglein, Phys. Lett. B **710**, 201 (2012) [arXiv:1112.3026 [hep-ph]]; A. Arbey, M. Battaglia, A. Djouadi, F. Mahmoudi and J. Quevillon, Phys. Lett. B **708** (2012) 162 [arXiv:1112.3028 [hep-ph]]; P. Draper, P. Meade, M. Reece and D. Shih, Phys. Rev. D **85**, 095007 (2012) [arXiv:1112.3068 [hep-ph]]; S. Akula, B. Altunkaynak, D. Feldman, P. Nath and G. Peim, Phys. Rev. D **85** (2012) 075001 [arXiv:1112.3645 [hep-ph]]; M. Kadastik, K. Kannike, A. Racioppi and M. Raidal, JHEP **1205** (2012) 061 [arXiv:1112.3647 [hep-ph]]; J. Cao, Z. Heng, D. Li and J. M. Yang, Phys. Lett. B **710** (2012) 665 [arXiv:1112.4391 [hep-ph]]; N. Karagiannakis, G. Lazarides and C. Pallis, arXiv:1201.2111 [hep-ph]; L. Aparicio, D. G. Cerdeno and L. E. Ibanez, JHEP **1204**, 126 (2012) [arXiv:1202.0822 [hep-ph]]; J. Ellis and K. A. Olive, Eur. Phys. J. C **72**, 2005 (2012) [arXiv:1202.3262 [hep-ph]]. H. Baer, V. Barger and A. Mustafayev, JHEP **1205** (2012) 091 [arXiv:1202.4038 [hep-ph]]; C. Balazs, A. Buckley, D. Carter, B. Farmer and M. White, arXiv:1205.1568 [hep-ph]; D. Ghosh, M. Guchait, S. Raychaudhuri and D. Sengupta, arXiv:1205.2283 [hep-ph].

8. C. Strege, G. Bertone, D. G. Cerdeno, M. Fornasa, R. R. de Austri and R. Trotta, JCAP **1203** (2012) 030 [arXiv:1112.4192 [hep-ph]].
9. P. Bechtle, T. Bringmann, K. Desch, H. Dreiner, M. Hamer, C. Hensel, M. Kramer and N. Nguyen *et al.*, JHEP **1206**, 098 (2012) [arXiv:1204.4199 [hep-ph]].
10. A. Fowlie, M. Kazana, K. Kowalska, S. Munir, L. Roszkowski, E. M. Sessolo, S. Trojanowski and Y. -L. S. Tsai, arXiv:1206.0264 [hep-ph].
11. T. Li, J. A. Maxin, D. V. Nanopoulos and J. W. Walker, arXiv:1206.2633 [hep-ph] and references therein.
12. ATLAS Collaboration, `https://cdsweb.cern.ch/record/1432199/files/ATLAS-CONF-2012-033.pdf`.
13. S. Chatrchyan *et al.* [CMS Collaboration], arXiv:1207.1798 [hep-ex], arXiv:1207.1898 [hep-ex].
14. O. Buchmueller *et al.*, Phys. Lett. B **657** (2007) 87 [arXiv:0707.3447 [hep-ph]].
15. O. Buchmueller *et al.*, JHEP **0809** (2008) 117 [arXiv:0808.4128 [hep-ph]].
16. O. Buchmueller *et al.*, Eur. Phys. J. C **64** (2009) 391 [arXiv:0907.5568 [hep-ph]].
17. O. Buchmueller *et al.*, Phys. Rev. D **81** (2010) 035009 [arXiv:0912.1036 [hep-ph]].
18. O. Buchmueller *et al.*, Eur. Phys. J. C **71** (2011) 1583 [arXiv:1011.6118 [hep-ph]].
19. O. Buchmueller *et al.*, Eur. Phys. J. C **71** (2011) 1634 [arXiv:1102.4585 [hep-ph]].
20. O. Buchmueller *et al.*, Eur. Phys. J. C **71** (2011) 1722 [arXiv:1106.2529 [hep-ph]].
21. G. Aad *et al.* [ATLAS Collaboration], arXiv:1204.0735 [hep-ex].
22. T. Aaltonen *et al.* [CDF Collaboration], Phys. Rev. Lett. **107**, 239903 (2011) [Phys. Rev. Lett. **107**, 191801 (2011)] [arXiv:1107.2304 [hep-ex]]; updated results presented at Aspen in Feb. 2012 by M. Rescigno, `https://indico.cern.ch/getFile.py/access?contribId=28&sessionId=7&resId=1&materialId=slides&confId=143360`.
23. S. Chatrchyan *et al.* [CMS Collaboration], Phys. Rev. Lett. **107**, 191802 (2011) [arXiv:1107.5834 [hep-ex]].
24. R. Aaij *et al.* [LHCb Collaboration], Phys. Lett. B **699** (2011) 330 [arXiv:1103.2465 [hep-ex]]; arXiv:1203.4493 [hep-ex].
25. For an official combination of the ATLAS, CMS and LHCb results, see: ATLAS, CMS, and LHCb Collaborations, `http://cdsweb.cern.ch/record/1452186/files/LHCb-CONF-2012-017.pdf`.
26. S. Chatrchyan *et al.* [CMS Collaboration], Phys. Lett. B **713**, 68 (2012) [arXiv:1202.4083 [hep-ex]].
27. E. Aprile *et al.* [XENON100 Collaboration], arXiv:1207.5988 [astro-ph.CO]].
28. For a description of `Delphes`, written by S. Ovyn and X. Rouby, see `http://www.fynu.ucl.ac.be/users/s.ovyn/Delphes/index.html`.
29. G. Bennett et al. [The Muon g-2 Collaboration], *Phys. Rev. Lett.* **92** (2004) 161802,

[arXiv:hep-ex/0401008]; and *Phys. Rev.* **D 73** (2006) 072003 [arXiv:hep-ex/0602035].
30. For a recent theoretical analysis within the Standard Model, see: F. Jegerlehner and R. Szafron, Eur. Phys. J. C **71** (2011) 1632 [arXiv:1101.2872 [hep-ph]].
31. The Heavy Flavor Averaging Group, D. Asner *et al.*, arXiv:1010.1589 [hep-ex], with updates available at `http://www.slac.stanford.edu/xorg/hfag/osc/end_2009`.
32. E. Aprile *et al.* [XENON100 Collaboration], Phys. Rev. Lett. **107**, 131302 (2011) [arXiv:1104.2549 [astro-ph.CO]].
33. ALEPH, CDF, D0, DELPHI, L3, OPAL, SLD Collaborations, the LEP Electroweak Working Group, the Tevatron Electroweak Working Group and the SLD electroweak and heavy flavour groups, arXiv:1012.2367 [hep-ex], as updated in March 2012 on `http://lepewwg.web.cern.ch/LEPEWWG/`.
34. Tevatron Electroweak Working Group for the CDF and D0 Collaborations, arXiv:1107.5255 [hep-ex].
35. ATLAS Collaboration, `https://atlas.web.cern.ch/Atlas/GROUPS/PHYSICS/CONFNOTES/ATLAS-CONF-2011-132/ATLAS-CONF-2011-132.pdf`.
36. J. Incandela, talk on behalf of the CMS Collaboration at CERN, 4th July, 2012, `https://cms-docdb.cern.ch/cgi-bin/PublicDocDB//ShowDocument?docid=6125`; CMS Collaboration, `http://cdsweb.cern.ch/record/1460438/files/HIG-12-020-pas.pdf`.
Our analysis does not use the results published more recently by the CMS Collaboration.
37. F. Gianotti, talk on behalf of the ATLAS Collaboration at CERN, 4th July, 2012, `https://cms-docdb.cern.ch/cgi-bin/PublicDocDB//ShowDocument?docid=6126`; ATLAS Collaboration, `http://cdsweb.cern.ch/record/1460439/files/ATLAS-CONF-2012-093.pdf`; `https://atlas.web.cern.ch/Atlas/GROUPS/PHYSOFFICE/higgs-preview.pdf`.
38. T. Aaltonen *et al.* CDF and D0 Collaborations], arXiv:1207.6436 [hep-ex].
39. G. Aad *et al.* [ATLAS Collaboration], Phys. Lett. B **710** (2012) 49 [arXiv:1202.1408 [hep-ex]].
40. S. Chatrchyan *et al.* [CMS Collaboration], Phys. Lett. B **710** (2012) 26 [arXiv:1202.1488 [hep-ex]].
41. For more information and updates, please see `http://cern.ch/mastercode/`.
42. S. Heinemeyer *et al.*, JHEP **0608** (2006) 052 [arXiv:hep-ph/0604147]; S. Heinemeyer, W. Hollik, A. M. Weber and G. Weiglein, JHEP **0804** (2008) 039 [arXiv:0710.2972 [hep-ph]].
43. B. C. Allanach, Comput. Phys. Commun. **143** (2002) 305 [arXiv:hep-ph/0104145].
44. G. Degrassi, S. Heinemeyer, W. Hollik, P. Slavich and G. Weiglein, Eur. Phys. J. C **28** (2003) 133 [arXiv:hep-ph/0212020]; S. Heinemeyer, W. Hollik and G. Weiglein, Eur. Phys. J. C **9** (1999) 343 [arXiv:hep-ph/9812472]; S. Heinemeyer, W. Hollik and G. Weiglein, Comput. Phys. Commun. **124** (2000) 76 [arXiv:hep-ph/9812320]; M. Frank *et al.*, JHEP **0702** (2007) 047 [arXiv:hep-ph/0611326]; See `http://www.feynhiggs.de` .
45. G. Isidori and P. Paradisi, Phys. Lett. B **639** (2006) 499 [arXiv:hep-ph/0605012]; G. Isidori, F. Mescia, P. Paradisi and D. Temes, Phys. Rev. D **75** (2007) 115019 [arXiv:hep-ph/0703035], and references therein.
46. G. Belanger, F. Boudjema, A. Pukhov and A. Semenov, Comput. Phys. Commun. **176** (2007) 367 [arXiv:hep-ph/0607059]; Comput. Phys. Commun. **149** (2002) 103 [arXiv:hep-ph/0112278]; Comput. Phys. Commun. **174** (2006) 577 [arXiv:hep-ph/0405253].
47. P. Skands *et al.*, JHEP **0407** (2004) 036 [arXiv:hep-ph/0311123]; B. Allanach *et al.*, Comput. Phys. Commun. **180** (2009) 8 [arXiv:0801.0045 [hep-ph]].
48. F. Mahmoudi, Comput. Phys. Commun. **178** (2008) 745 [arXiv:0710.2067 [hep-ph]]; Comput. Phys. Commun. **180** (2009) 1579 [arXiv:0808.3144 [hep-ph]]; D. Eriksson, F. Mahmoudi and O. Stal, JHEP **0811** (2008)

035 [arXiv:0808.3551 [hep-ph]].
49. Information about this code is available from K. A. Olive: it contains important contributions from T. Falk, A. Ferstl, G. Ganis, F. Luo, A. Mustafayev, J. McDonald, K. A. Olive, P. Sandick, Y. Santoso and M. Srednicki.
50. P. Gondolo, J. Edsjo, P. Ullio, L. Bergstrom, M. Schelke and E. A. Baltz, JCAP **0407** (2004) 008 [astro-ph/0406204]; P. Gondolo, J. Edsj, P. Ullio, L. Bergstrom, M. Schelke, E.A. Baltz, T. Bringmann and G. Duda, `http://www.darksusy.org`.
51. R. Aaij *et al.* [LHCb Collaboration], arXiv:1205.3422 [hep-ex].
52. J. P. Lees *et al.* [BaBar Collaboration], arXiv:1205.5442 [hep-ex].
53. S. Chatrchyan *et al.* [CMS Collaboration], Phys. Rev. Lett. **107**, 221804 (2011) [arXiv:1109.2352 [hep-ex]].
54. T. Sjostrand, S. Mrenna and P. Z. Skands, Comput. Phys. Commun. **178** (2008) 852 [arXiv:0710.3820 [hep-ph]].
55. J. Ellis, K. Olive and Y. Santoso, Phys. Lett. B **539**, 107 (2002) [arXiv:hep-ph/0204192]; J. R. Ellis, T. Falk, K. A. Olive and Y. Santoso, Nucl. Phys. B **652**, 259 (2003) [arXiv:hep-ph/0210205].
56. Y.-M. Yook for the Belle Collaboration, `http://indico.cern.ch/getFile.py/access?contribId=573&sessionId=66&resId=0&materialId=slides&confId=181298`.
57. A. J. Buras, M. V. Carlucci, S. Gori and G. Isidori, JHEP **1010** (2010) 009 [arXiv:1005.5310 [hep-ph]].
58. K. de Bruyn, R. Fleischer, R. Knegjens, P. Koppenburg, M. Merk and N. Tuning, arXiv:1204.1735 [hep-ph].
59. K. de Bruyn, R. Fleischer, R. Knegjens, P. Koppenburg, M. Merk, A. Pellegrino and N. Tuning, arXiv:1204.1737 [hep-ph].
60. See, for example: M. M. Pavan, I. I. Strakovsky, R. L. Workman and R. A. Arndt, PiN Newslett. **16** (2002) 110 [hep-ph/0111066]; and M. M. Pavan, private communication.
61. R. Barate *et al.* [ALEPH, DELPHI, L3, OPAL Collaborations and LEP Working Group for Higgs boson searches], Phys. Lett. B **565** (2003) 61 [arXiv:hep-ex/0306033].
62. S. Schael *et al.* [ALEPH, DELPHI, L3, OPAL Collaborations and LEP Working Group for Higgs boson searches], Eur. Phys. J. C **47** (2006) 547 [arXiv:hep-ex/0602042].
63. S. S. AbdusSalam, *et al.*, Eur. Phys. J. C **71**, 1835 (2011) [arXiv:1109.3859 [hep-ph]].